AMERICAN UNIVERSITY OF BEIRUT

OMNIDIRECTIONAL HUMANOID FALL AVOIDANCE STRATEGIES AND DECISION VOLUME

by

NOEL S. EL KHAZEN

A thesis
submitted in partial fulfillment of the requirements
for the degree of Master of Engineering
to the Department of Mechanical Engineering
of the Faculty of Engineering and Architecture
at the American University of Beirut

Beirut, Lebanon
August 2014

AMERICAN UNIVERSITY OF BEIRUT

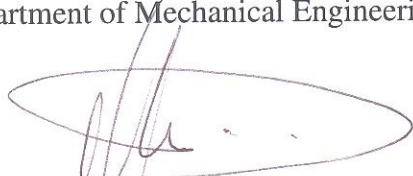## OMNIDIRECTIONAL HUMANOID FALL AVOIDANCE STRATEGIES AND DECISION VOLUME

by

NOEL S. EL KHAZEN

Approved by:

_____

Dr. Daniel Asmar, Associate Professor   Advisor
Department of Mechanical Engineering

_____

Dr. Imad Elhajj, Associate Professor   Member of Committee
Department of Electrical & Computer Engineering

_____

Dr. Najib Metni, Assistant Professor   Member of Committee
Department of Mechanical Engineering

Date of thesis defense: August 7 2014

AMERICAN UNIVERSITY OF BEIRUT

THESIS, DISSERTATION, PROJECT RELEASE FORM

Student Name: __El Khazen_____Noël_____Samir_____

                   Last   First   Middle

☒ Master's Thesis   ◯ Master's Project   ◯ Doctoral Dissertation

☒   I authorize the American University of Beirut to: (a) reproduce hard or electronic copies of my thesis, dissertation, or project; (b) include such copies in the archives and digital repositories of the University; and (c) make freely available such copies to third parties for research or educational purposes.

☐   I authorize the American University of Beirut, **three years after the date of submitting my thesis, dissertation, or project,** to: (a) reproduce hard or electronic copies of it; (b) include such copies in the archives and digital repositories of the University; and (c) make freely available such copies to third parties for research or educational purposes.

_____   September 15, 2012

Signature   Date

This form is signed when submitting the thesis, dissertation, or project to the University Libraries

ACKNOWLEDGEMENTS

AN ABSTRACT OF THE THESIS OF

Noel S. El Khazen   for   Master of Engineering
                            Major: Mechanical Engineering

Title: Omnidirectional Humanoid Fall Avoidance Strategies and Decision Volume

Our lives are becoming more and more dependent on different types of robots, such as cars, industrial robots, medical robots. Humanoids on the other hand, can easily be integrated into a human environment and perform some basic chores. For example, ASIMO robot developed by Honda can serve coffee on a tray and push a cart in an ordinary office. To accomplish a task in a dynamic environment such as an office, humanoids must be equipped with a fall avoidance protocol. This allows them to handle unexpected disturbances.

The contributions of this thesis are twofold. First I introduce what I call a decision volume, which is used to determine the states from which the robot can recover. The decision volume is an extension of what is previously known in the literature as the decision surface—limited to perturbations and states in the sagittal plane, to handle disturbances emanating from random directions in the azimuth plane. The second contribution is the extension of the ankle and hip strategies for humanoid fall avoidance to handle disturbances in random directions.

The robot is physically modeled as a 3D Linear Inverted Pendulum Model (LIPM) for the ankle strategy, and for the hip strategy a sphere is added. Using these models, the decision volumes are calculated analytically. After that to test their validity, both strategies are implemented using Virtual Model Control (VMC) in simulations and in the experiments on the real robot. The results show that the decision volume was successful in determining which strategy is applicable. For robot's states that are within the decision volume of the strategy the robot succeeds in keeping its balance, whereas for states that are outside the decision volume the robot falls down.

CONTENTS

ILLUSTRATIONS

ix

TABLES

CHAPTER I

INTRODUCTION

A. Humanoids

The industrial revolution was a turning point in the manufacturing processes. After that, our lives became more and more dependent on machinery and automated systems. In industry machines and robots replace humans and accomplish tasks that are repetitive, monotonous, contain a high level of risk, or need a high level of accuracy. For example, robotic arms are used in car industries for assembly, welding, and painting. Given the rapid development in humanoid robotics it is not unlikely that in the next decade or two we will have them as companions at work and at home. Having a human-like structure will ease the process of integrating humanoids into our environment. In addition, they will be able to perform human chores such as cleaning [3] and cooking [4]. Another example of a role that a humanoid can play, is to assist nurses to complete their daily tasks and provide a better health care [5].

No matter what are the duties that will be assigned to humanoids, to be a replacement for a human force, they need to acquire the essential ability of keeping their balance. This task is an easy task for a healthy adult and does not require much consciousness. Although it seems trivial to keep an upright position when pushed, this seemingly intuitive ability is difficult to understand and model. Our body mass is located two-thirds above the ground, thereby turning us into an inherently unstable systems that need constant control [6]. Humanoids also face the same challenges. So in order to better understand humanoids and biped systems we need to acquire a wider knowledge of ourselves.

For this reason, a lot of research is focused on understanding and implementing

1

this natural behavior to implement it on robots. According to Chiba [7], humans control their posture by controlling the muscle activity of the whole body using multi-sensory inputs. The main sensory information for balance control is provided by visual, vestibular, and somatosensory inputs. Winter [6] on the other hand claims that humans use their hips and ankles in order to maintain their balance during quiet standing.

B. Synopsis

This thesis deals with stability of bipedal robots in a quiet standing mode. Two strategies are inspired by human behavior and reflexes, which are the ankle strategy and the hip strategy. These strategies are developed to handle perturbations coming from different directions. I will present for each strategy an analytical stability volume, which will determine which strategy is sufficient to avoid falling. The control of our system is based on the Virtual Model Control [8]. It is used to handle disturbances coming from any direction.

To test this theory we worked with Webots simulator [9], which is based on the Open Dynamics Engine (ODE). Webots contains in its library many robots including NAO robot, which is the one, used in our simulations. The developed system is then implemented on a real NAO humanoid [10].

C. Motivation, Importance and Difficulties

Humans are bipedal systems, and a person may spend his entire life without understanding the system dynamics responsible of balancing and walking. If humanoids are to coexist with humans, it is essential to learn how to stay on their feet before performing any task. It is enough to watch a RoboCup game to see the need of such systems. During these games, a humanoid suffers from perturbations from different

directions and many times falls down. Although after hitting the ground the robot has a procedure to stand up and continue the game, it takes a relatively long period of time. In addition, when a robot falls it can cause damage to itself and to the environment around it. A fall may cause financial damage since these robots are expensive. Also it may be a health risk since some of these robot are heavy and may harm humans and cause injuries.

Many challenges face the bipedal robots. First of all, the dynamics of the system are non-linear and high dimensional. Then these systems are inherently unstable and finally the foot-ground interaction is complicated. In addition, another difficulty emerges when trying to implement these strategies on the real robot. Humanoids have limited processing power and increasing it comes at an increase in the cost of the robot. Therefore it is common that performance of the code execution is limited. Finally, many robots lack torque control. Instead, they are limited to position and velocity control.

To deal with these problems the system is simplified by taking the appropriate assumptions. According to Pratt [11], simplified models are used to overcome these difficulties. These models proved to be very useful for analysis and control. These assumptions make our system linear, and preserve on the other hand the properties of interest. For testing, a small-scale robot is used. This robot has an acceptable price and sufficient processing power to do the experiments.

D. Thesis Outline

The following chapters are organized as follows:

Chapter II gives a background, shows the kinematic model used for humanoids, and introduces previous models used in fall avoidance.

Chapter III is the literature review. This chapter discusses different approaches used to deal with fall avoidance. It shows the advantages and the disadvantages of each approach.

Chapter IV presents both ankle and hip strategies. The model used for these strategies is based on the 3D-LIPM. After that, the corresponding decision volumes for each strategy are computed. These decision volumes determine when the strategies are effective. Following that, the control is developed using VMC.

Chapter V shows the result of different simulations that are done. After succeeding in the simulation, the work was implemented on a real humanoid robot. In these experiments, the robot is pushed from different directions and the fall avoidance is insured by using one of the two strategies. In this chapter, the decision volume is also verified.

Chapter VI concludes the work done in this thesis and suggests future work and development.

CHAPTER II

A GENERAL OVERVIEW ON HUMANOIDS ROBOTS

This chapter presents the background regarding humanoid fall avoidance. First, the different human fall avoidance strategies are explained. After that, the robot's kinematics are discussed. Finally, the last section shows the different models used for fall avoidance. Bipedal robots differ from manipulators that possess a fixes base, in that they do not have a defined base. This is due to the ground foot interaction that cannot be taken for granted. In fact, the foot exerts a unilateral force and the foot can only exert a force in the downward direction. As a result, this interaction creates the effect of an under-actuated joint that causes the foot to rotate and tip over. Because of this complex interaction between the foot and the ground, the stability of the bipedal system becomes more challenging.

A. Fall Avoidance Strategies

This section discusses three fall avoidance strategies adopted by humans. The strategies are the ankle strategy, the hip strategy and the stepping strategy.
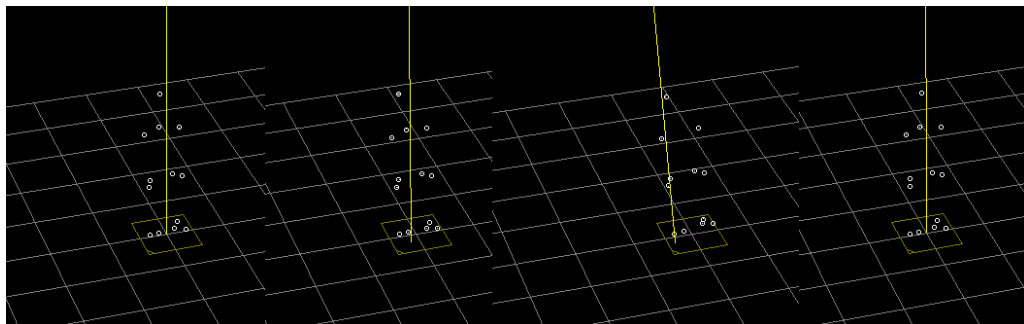
Figure 1: Ankle strategy used by an individual to recover from a push

Ankle Strategy: In this strategy only the ankles are involved to keep the body

in balance. Humans always use the ankle's muscles while in quiet standing since we are inherently unstable system [26]. The foot-ground interaction poses a limitation on the amount of torque that the ankles can provide. For that reason, this strategy is useful for relatively small disturbances. Using the Vicon system [reference here], and to better understand the human motion, we tracked the reaction of a human subject after being pushed. Fig. 1 shows the reaction of an individual when he is pushed from his left side with a 45° angle. Only the movement of the lower body parts is recorded. The main joint that was involved in restoring the balance was the right ankle joint.

Hip Strategy: is also called momentum strategy. This strategy is also used by humans. It involves rotation of the torso and other limbs such as the hands. This action creates momentum that reduces the effect of a push. In general, this strategy involves both hips and ankles. A temporal snapshot of the human reflex is shown in Fig. 2. Here the human is represented by a stick model shown from the front. The yellow arrow represents the direction of the push. The red lines represent the torso and hips. The legs are represented by green lines. During this strategy, only one foot is involved, while the other one is in the air. Also, through this reaction knees are locked and do not have any contribution to the fall avoidance strategy.
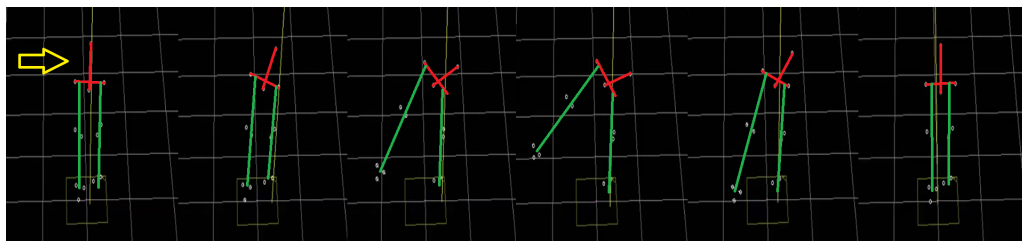
Figure 2: Hip strategy used by an individual to recover from a push

Stepping Strategy: This strategy handles perturbation that are much larger and cannot be handled by the previous two strategies. In that case an individual make take on or several steps to recover from a disturbance.

In what follows we will give a small description on some of the previous work done by different researchers on fall avoidance.

B. Humanoid Kinematics

The kinematics of a humanoid shares some characteristics of a robotic arm, such as the fact that the coupling between its links is nonlinear. Although these similarities exist, some differences can be noted.

First of all, a humanoid is a multi-chain mechanism, whereas a robotic arm consists of a single chain. In general, the configuration of a humanoid is described in a 3D space by decomposing the problem into five independent parts, which are the head, the two legs, and the two hands [12]. Then the CoM, which is typically located at the torso, is used as the base for each of the five chains. The CoM position is described in the world frame then its different chains are expressed relative to the CoM. This method is widely used in mobile robotics locomotion. In our case, since the robot remains at its place and only the legs are actuated, two chains are taken into consideration. These chains correspond to both the left and the right legs, which present the support for the CoM.

After that, the end-effector is the robot's end that needs to be accurately moved to perform a certain task such as welding in the case of a robotic arm. For humanoids, the end-effector can be the CoM, a foot, or any other limb. For example, in the humanoid locomotion the foot needs to be placed on the ground with a defined location, in that case the end effector is the foot. In our case, the end-effector is at the CoM because its motion is examined with respect to its supports.

Finally, the last difference between a humanoid and a manipulator is the base type. In the case of a robotic arm, the base is fixed, whereas for a humanoid it is not. The ground foot interaction makes the system more complex. The foot rotation increases the DoF of a humanoid system.

In what follows, the upper body of the robot will be replaced by its CoM. The head, the hands, and the torso will be considered as one block. The mass of the legs are neglected. Fig. 3 shows the CoM as a black circle. The lower body is similar to that of

7

humans with a small variation. This diagram disregards the knees joints. Through our work the knees are kept stiff and do not have any contribution to our system. As a result, each leg consists of four joints; namely the ankle and hip roll and pitch motors. This results in a system with a total of 4-DoF. The z-axis in the Fig. 3 of frame $\{1\}$ to $\{4\}$ is the rotation axes of the motors. As for the angles of these rotational joints, the following nomenclature is used. First of all, a and h denote the angle of the ankles and hips respectively. After that, subscript L and R denote the leg side that the motor belongs to. Finally, the motor type is added whether it is a pitch motor or a roll motor. For example, a_{Lpitch} denotes the angle of the ankle pitch motor of the left leg.
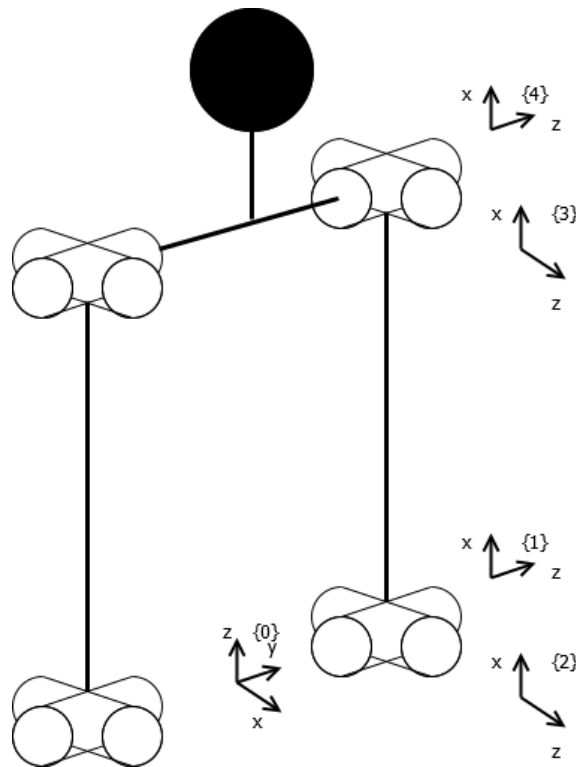
Figure 3: The 8-Dof Model

1. Denavit-Hartenberg parameters

Denavit-Hartenberg (DH) parameters are widely used in robotics to describe the relation between links of a given chain. These parameters are used to compute the

transformation matrix that transform the coordinates of a point expressed in a frame of one end of a link, to the other end in function of the joint state. The DH parameters, that are described by Craig [2], are as follows: the link length a, the link twist α, the link offset d and the joint angle θ. Before deducing these parameters, the frames $\{1\}$ to $\{4\}$ are placed as follows for a joint i:

- The z_i-axis is along the joint rotation axis.

- The x_i-axis is pointing along the common perpendicular of z_i and z_{i+1}.

- The y_i-axis is placed to complete the right-hand coordinate system formed by x_i and z_i.

After attaching the frames and following the previous definitions, the link parameters are expressed as follows:

- a_{i-1} is the distance from z_{i-1}-axis to z_i-axis along x_{i-1}-axis.

- α_{i-1} is the angle from z_{i-1}-axis to z_i-axis along x_{i-1}-axis.

- d_i is the distance from x_{i-1}-axis to x_i-axis measured along z_i-axis.

- θ_i is the angle from x_{i-1}-axis to x_i-axis measured about z_i-axis.

$^{i-1}_{i}T$ is the transformation that goes from frame $\{i\}$ to $\{i-1\}$ and it is equal to,

$$
^{i-1}_{i}T = \begin{bmatrix} \cos\theta_i & -\sin\theta_i & 0 & a_{i-1} \\ \sin\theta_i\cos\alpha_{i-1} & \cos\theta_i\cos\alpha_{i-1} & -\sin\alpha_{i-1} & -\sin\alpha_{i-1}d_i \\ \sin\theta_i\sin\alpha_{i-1} & \cos\theta_i\sin\alpha_{i-1} & -\cos\alpha_{i-1} & -\cos\alpha_{i-1}d_i \\ 0 & 0 & 0 & 1 \end{bmatrix}. \tag{1}
$$

2. Transformation Matrices

In this section, the robot's kinematics are developed by considering one of the two chains, depending on the legs. It is a must that the chain chosen must pass through the leg that is in contact with the ground. Table 1 shows the DH-parameters in the case where the left leg is the leg that is in contact with the ground. The chain selected, starts from frame {0} and ends at frame {4}. The frame {0} is the world frame. It is placed in the middle of the line that passes through the ankle pitch motors axis. Whereas the frame {4} is connected to the last joint, which is the hip.

Table 1: Modified-DH parameters using Craig's convention [2]

i	α_{i-1}	a_{i-1}	d_i	θ_i
1	$-pi/2$	0	L_{wa}	$a_{Lpitch} - \pi/2$
2	$-pi/2$	0	0	a_{Lroll}
3	0	L_{ah}	0	h_{Lroll}
4	$pi/2$	0	0	h_{Lpitch}

L_{wa} is the distance between the world frame and the left ankle. L_{ah} is the distance between the ankle and the hip.

The matrix in (1) is used to find the transformations from a frame to the previous one. Finally, the transformation from {4} to {0} is found by multiplying the transformation matrices as follows,

$$_4^0T = {}_0^1T \, {}_1^2T \, {}_2^3T \, {}_3^4T. \tag{2}$$

$_4^0T$ will have the following form,

$$_4^0T = \left[\begin{array}{ccc|c} & _4^0R & & ^0P_{4ORG} \\ \hline 0 & 0 & 0 & 1 \end{array} \right]. \tag{3}$$

10

Where ^0_4R is a 3×3 rotation matrix. ^0_4R is the rotation of the frame {4} expressed in the frame {0}. $^0P_{4ORG}$ is a 3×1 position vector. $^0P_{40ORG}$ is the origin of the frame {4} expressed in the frame {0}.

To find the CoM coordinates in the world frame first it should be expressed in the frame {4},

$$^4P_{CoM} = \begin{bmatrix} L_{torso} \\ 0 \\ -L_{wa} \end{bmatrix}. \tag{4}$$

L_{torso} is the vertical distance between the hips and the CoM. Then the position vector of the CoM is multiplied by the transformation matrix (5),

$$\begin{bmatrix} ^0P_{CoM} \\ 1 \end{bmatrix} = {}^0_4T \begin{bmatrix} ^4P_{CoM} \\ 1 \end{bmatrix} = \left[\begin{array}{c|c} ^0_4R & ^0P_{4ORG} \\ \hline 0 \quad 0 \quad 0 & 1 \end{array} \right] \begin{bmatrix} L_{torso} \\ 0 \\ -L_{wa} \\ 1 \end{bmatrix}. \tag{5}$$

The coordinates of the CoM expressed in the world frame are shown in (6), (7) and (8).

$$\begin{aligned} x_{CoM} \quad = \quad & L_{torso}\cos a_{Lpitch}\sin h_{Lpitch} + L_{ah}\cos a_{Lroll}\sin a_{Lpitch} \\ & -L_{wa}\cos h_{Lroll}\sin a_{Lpitch}\sin a_{Lroll} - L_{wa}\cos a_{Lroll}\sin h_{Lroll}\sin a_{Lpitch} \\ & -L_{torso}\cos h_{Lpitch}\sin h_{Lroll}\sin a_{Lpitch}\sin a_{Lroll} \\ & +L_{torso}\cos h_{Lroll}\cos h_{Lpitch}\cos a_{Lroll}\sin a_{Lpitch} \end{aligned} \tag{6}$$

$$\begin{aligned} y_{CoM} \quad = \quad & L_{wa} - L_{wa}\cos(h_{Lroll} + a_{Lroll}) - L_{ah}\sin a_{Lroll} \\ & -L_{torso}\sin(h_{Lroll} + a_{Lroll})\cos h_{Lpitch} \end{aligned} \tag{7}$$

$$
\begin{aligned}
z_{CoM} \;=\;& L_{ah}\cos a_{Lpitch}\cos a_{Lroll} - L_{torso}\sin h_{Lpitch}\sin a_{Lpitch} \\
& - L_{wa}\cos h_{Lroll}\cos a_{Lpitch}\sin a_{Lroll} - L_{wa}\cos a_{Lpitch}\cos a_{Lroll}\sin h_{Lroll} \\
& - L_{torso}\cos h_{Lpitch}\cos a_{Lpitch}\sin h_{Lroll}\sin a_{Lroll} \\
& + L_{torso}\cos h_{Lroll}\cos h_{Lpitch}\cos a_{Lpitch}\cos a_{Lroll}
\end{aligned}
\tag{8}
$$

C. Dynamic Model

To deal with the different complexities of a humanoid system, many dynamic models are developed. This simplifies the problem and the system can be better understood [13]. A simplified dynamic model conserves the characteristics of interest.

1. Humanoid Stability

First, we need to define stability of a humanoid system. A humanoid is said to be stable when it will not fall. Although this definition is general and can be interpreted in many ways, the contact with the ground must only be with the feet and no other point must touch the ground or else the system will be unstable [14]. Others defined stability as keeping the flat foot fully in contact with the ground [15]. In this case, the robot control becomes similar to that of a manipulator with a fixed base. The foot ground contact is not always guaranteed, it is affected by the upper body dynamics. Undesired upper body movement may cause the foot to partially or completely lose the contact with the ground and cause the robot to fall. The robot stability is divided into two parts. The first one is the stability during quiet standing. The robot uses its ankles, hips or even takes a step to keep its balance. The second part is the stability during walking. Although stable gates are developed, the robot may be exposed to perturbation. Renner *et al.*proposed a method to detect perturbation during walking [16]. They tackled this problem by differentiating between small and large instabilities. For small

instabilities, slowing down the robot is enough. Whereas for stronger instabilities the robot should stop then be brought back into a stable posture with a lower center of mass. Finally walking continues after the instability disappears.

In our work, only stability during quiet standing is discussed. The robot uses its ankles and hip to recover. After applying the strategies, the robot returns to its initial position.

2. *Foot Ground Interaction: CoP, ZMP and FZMP*

The foot of a humanoid may rotate around any edge. This creates an additional DoF. Although this DoF is not actuated, it is influenced by the forces and moments that are generated by the upper body dynamics. The humanoid foot can only push the ground and it is not pinned to it. These factors are responsible for the instability of a humanoid. Although the factors allow humanoid locomotion, they make the robot hard to control. To deal with this problem researchers introduced the center of pressure (CoP), zero moment point (ZMP), and fictitious zero moment point (FZMP).

Center of Pressure (CoP) is located on the ground under the area covered by the foot. The field of pressure forces under the foot can be replaced by a single force, which is the normal resultant force, located at a point where the resultant moment is zero [17]. The resultant normal force is $R_n = \int_A p_n dA$, where p_n is the normal pressure distributed under the area A. Fig. 4 shows an example of stress distribution in the sagittal plane. The location of the CoP is $OP = \frac{\int x p_n(x) dx}{\int p_n(x) dx}$. When the CoP is closer to the foot edge, the robot becomes less stable. Humans can experience the movement of the CoP, and all they need to do is to stand up and move their body mass. By doing this experiment, they feel a pressure point that moves along their foot.

P_L and P_R respectively denote the CoP of the left and the right foot. From these two points a common CoP can be located within the support polygon and not limited to
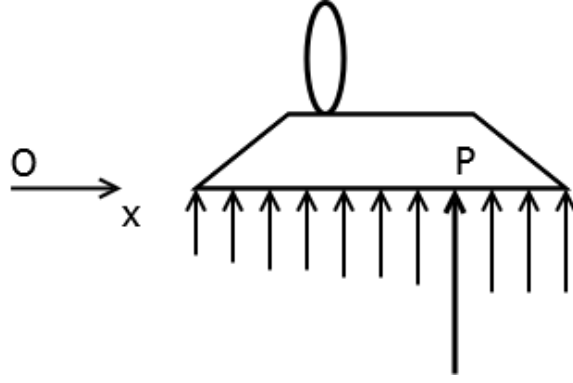
Figure 4: Normal stress distribution under the foot.

one of the two foot soles.
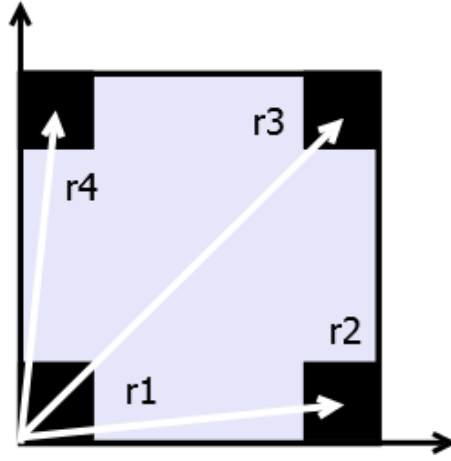
Figure 5: Force sensitive resistors distribution.

The CoP can be practically calculated using Force Sensitive Resistors (FSR). The sensors are shown in Fig. 5. In (9), r_i represents the position of the ith sensor and f_i represents the value of the force at the ith sensor. The CoP will be located according to

$$OP = \frac{\sum\limits_{i=1}^{4} f_i r_i}{\sum_{i=1}^{4} r_i}.$$ (9)

Zero Moment Point (ZMP), is the location on the ground where the robot's inertial, gravitational, Coriolis, and centrifugal forces are balanced by the reaction force [18]. The concepts of COP and ZMP are used together in order to establish the stability of a humanoid. If the ZMP is inside the foot soles, the COP has to follow the

14

ZMP in order for the system to be brought back to equilibrium. If the ZMP position exceeds the foot sole, the robot should take action (such as the momentum strategy or take a step) in order to bring the ZMP back inside the region where a reaction force at the CoP keeps the humanoid from falling down. To compute the ZMP the cart-table model can be used [1]. The model in Fig. 6 is a simple way to compute the ZMP. In this model, the mass is kept at a constant high.
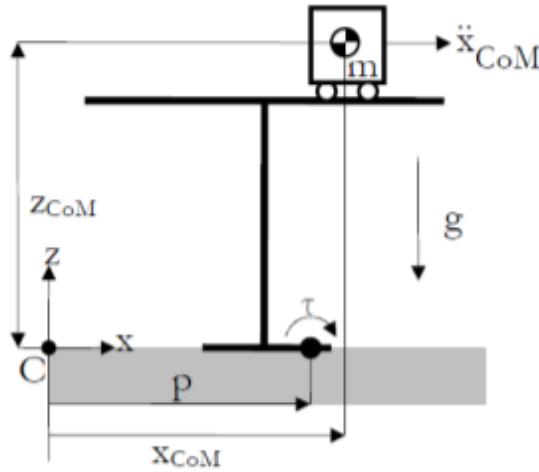
Figure 6: Cart-table model [1]

$$p_x = x_{CoM} - \frac{\ddot{x}_{CoM}}{g} z_{CoM}, \tag{10}$$

$$p_y = y_{CoM} - \frac{\ddot{y}_{CoM}}{g} z_{CoM}. \tag{11}$$

p_x and p_y of (10) and (11) are the coordinates of the ZMP. z_{CoM} is the height of the CoM and g is the gravitational acceleration.

Fictitious Zero Moment Point (FZMP) is also called foot rotation indicator (FRI). This point is where the reaction force must be located to keep the foot at its place. When the ZMP exceeds the support polygon it becomes a FZMP, where the reaction force should be. In this case, the CoP is kept at the support polygon edge where the reaction force is located. The difference between the CoP and the FZMP causes a tipping moment.

3. Simplified Humanoid Models

Linear Inverted Pendulum Model shown in Fig. 7 was first introduced by Hemami *et al.*[19]. The different parts and masses of the body are replaced by a point mass located at the CoM. The only joint that is actuated is the ankle joint. As a result, the dynamic equation becomes

$$mL^2\ddot{\theta} = mgL\sin\theta - T_a,\tag{12}$$

where T_a is the ankle torque, L is the pendulum length and m is the mass of the CoM. Although (12) is not linear, it is linearized by assuming a small angle θ. Thus $\sin\theta$ is replaced by θ.

Figure 7: Linear Inverted Pendulum Model

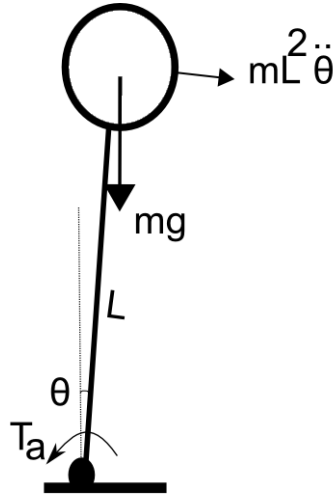Kajita and Tani [20] modified the previous model by increasing its degree of freedom by one. They added a prismatic joint as shown in Fig. 8. This joint keeps the CoM at a constant height thus making the system linear. The system dynamics can be expressed in the following formula

$$\ddot{x}_{CoM} = \frac{g}{z_c}x_{CoM} + \frac{1}{mz_c}\tau_a.\tag{13}$$

16

In (13) m is the pendulum mass, τ_a the ankle torque along y-axis and z_c is the constant height of the CoM. It is clear that the equation of the LIPM (13) is linear.

Figure 8: Linear Inverted Pendulum Model with a prismatic joint

Then Kajita *et al.* [21] introduced the 3D Linear Inverted Pendulum Model (3D-LIPM) to generate walking patterns for humanoids and cover robot motion in 3D. In this model, the CoM is kept at constant height.

Angular Momentum Pendulum Model is the model used in general for the hip strategy. The AMPM [22] takes into consideration the rotation of the torso. Although this model is similar to the LIPM, previously discussed, it adds to the point mass placed on the stick, an inertia. According to Kudoh and Kumar [23] a momentum can be generated by applying a torque to the torso. The rotation of the upper body is simulated by a flywheel [24]. Fig. 9 shows the angular momentum pendulum model.

Having an additional input the system can be modeled by these equations,

$$\ddot{\theta} = \frac{g}{L}\theta - \frac{T_a}{mL^2} - \frac{T_b}{mL^2}, \tag{14}$$

$$T_b = J\ddot{\beta}. \tag{15}$$

Although the disc will rotate in the clockwise direction, the momentum generated will create a torque in the counterclockwise direction. This is the reason for having an additional torque T_b in (14) that has the same effect of the ankle torque T_a. T_b
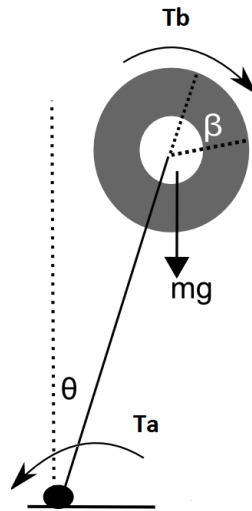
Figure 9: Angular Momentum Pendulum Model (AMPM)

is the torque responsible of the flywheel acceleration. J is the flywheel inertial and β is the flywheel angular position. Pratt *et al.* [25] used a modified version of this model. They added a prismatic joint to the pendulum to keep the CoM at a constant height.

The model used in this thesis is based on the 3D-LIPM. This model covers the motion of the CoM in x and y directions. In this model, the CoM is kept at a constant height. Finally to simulate the hip joints, a sphere is added.

CHAPTER III

FALL AVOIDANCE FOR HUMANOIDS

A. Literature Review

1. Capture Point

Pratt *et al.* [27, 28] developed the capture point. It represents a point on the ground where the robot can step to in order to bring itself to a complete stop. Depending on the capture point location, a robot may use its ankles, hips, or even take one or several steps to recover. The capture point is expanded to a capture region by actuating the hip joint [25]. As a result, instead of having a point to step into, there is a region. Failing to reach the capture point or region causes the robot to fall. This is caused by the kinematic constraints of the robot. Pratt *et al.* [11] derived the capture point using the concept of orbital energy for a LIP. The energy equation is

$$E_{LIP} = \frac{1}{2}\dot{x}^2 - \frac{g}{2z_c}x^2. \tag{16}$$

where E_{LIP} is the Linear Inverted Pendulum energy, x is the horizontal displacement from the foot to the CoM, $\dot{x}$ is the velocity, z_c is the constant height of the CoM and g is the gravitational acceleration. According to Pratt E_{LIP} has three states. If $E_{LIP} < 0$ then the CoM will stop and reverse the direction before reaching the foot edge. If $E_{LIP} > 0$ the orbital energy is enough to reach the foot edge, then accelerate and continue in its way. Finally if $E_{LIP} = 0$ the CoM will come at rest,as a result

$$x_{capture} = \dot{x}\sqrt{\frac{z_c}{g}}. \tag{17}$$

After the capture point is computed, Pratt expanded this concept to a capture region. This is done by replacing the point mass by a flywheel thus the strategy becomes the momentum strategy. By changing the model, new constraints arise. The first one is the torque applied on the flywheel. The torque is limited by the motors. After that, the wheel cannot rotate indefinitely. For that reason, the wheel accelerates then decelerates and stops before exceeding the maximum angular position. On the other hand, the capture point computed is an instantaneous capture point. The capture point is not fixed but it varies in function of time. This means, while the robot tries to reach the capture point, this point may change its place. This is caused by the robot dynamics.

Pratt [29] presented a method to learn the capture point. The LIPM previously used is not accurate enough for real life implementation. The assumptions made on the LIPM result in errors that cause the robot to step into the wrong place. The learning method proposed by Pratt, is based on the learning offsets of the capture points predicted by the LIPM. This is used instead of the dynamic model reduces the rate of failure.

2. *Decision Surface*

Stephens [30] originally developed the decision surface for the ankle strategy, then followed by Jalgha *et al.*[31, 32] and Asmar *et al.*[33] for the hip strategy. Having the initial states (position and velocity) of the robot, the decision surface is able to determine whether the robot is able to recover from a push, and which strategy is appropriate to use. Jalgha *et al.*also implemented the strategies on a humanoid using Virtual Model Control (VMC) [8].

Deciding when to apply which fall avoidance strategy is based on a model that is developed for each strategy, which is capable of inferring from the current state (angular position and angular velocity) of the humanoid if it can recover by applying the corresponding strategy. The decision surface, introduced by Stephens [30], delineates the

thresholds (or 2D region if we consider a 2DoF robot) beyond which the robot cannot avoid falling by applying the corresponding fall avoidance strategy. The procedure to determine the decision surface is to consider first a disturbance that drives the system to the border of stability. At this state the CoP reaches the edge of the foot and $T_a = -mg\delta$, where δ is the distance from the ankle joint to the edge of the foot. The initial values of θ and $\dot{\theta}$ for which the CoP reaches the edge of the foot delineates the borders of our decision surface. Jalgha $et\ al.$[32] found this region to be specified as:

$$f^- < \theta_0 + \frac{\dot{\theta}_0}{\omega} < f^+, \tag{18}$$

where $f^{\pm} = \delta^{\pm}/L$. Anytime θ and $\dot{\theta}$ of the system gets beyond this decision surface area the ankle strategy is no longer capable of preventing the robot from falling and an alternate solution such as a momentum strategy is required. The momentum strategy generates an additional torque that assists in balance recovery. This strategy, due to the previously limitation mentioned, is applied for a determined period of time. Hence, after it is done it should place the robot within the decision surface of the ankle.

$$f^- < \theta(2t_1) + \frac{\dot{\theta}(2t_1)}{\omega} < f^+, \tag{19}$$

where $\theta(2t_1)$ and $\dot{\theta}(2t_1)$ are the states after the momentum strategy is fully exploited. The time $2t_1$ is the time needed to accomplish full hip strategy. As a result, the decision volume becomes,

$$f^- < e^{2\omega t_1}\theta_0 + \frac{e^{2\omega t_1}}{\omega}\dot{\theta}_0 - \frac{T_{bm}}{mL^2\omega^2}\left[e^{2\omega t_1} - 2e^{\omega t_1} + 1\right] < f^+, \tag{20}$$

where T_{bm} is the maximum hip torque and ω is $\sqrt{\frac{g}{m}}$.

Although the decision surface is appropriate for each robot configuration and is not time dependent, it is limited to disturbances in the coronal or sagittal planes.

3. Reaction Null Space Method

Nishio *et al.* [34, 35], proposed a balance control method based on the reaction null space method, which is originally developed to handle base disturbances of free-flying robots [36]. It can be applied directly for balance recovery of a humanoid under the hip strategy. The motion of the links creates a force on the base. Whether the base is in space or on the ground, the reaction force can be controlled to avoid unwanted results. In space, the motion of the manipulator is optimized to reduce the disturbance on the base. In the case of a humanoid, the foot is considered as the base and the rest of the links are treated as the manipulator in the previous case. The joint speeds are then computed by conserving the coupling momentum.

$$\dot{\theta}_1 = \frac{-m_2 l_{g2} C_{12}}{(m_1 l_{g1} + m_2 l_1) C_1 + m_2 l_{g2} C_{12}} \dot{\theta}_2 \qquad (21)$$

The relation between the angular speed of the ankle joint ($\dot{\theta}_1$) and that of the hip joint ($\dot{\theta}_2$) are shown in (21). $C_1 = \cos\theta_1$ and $C_{12} = \cos(\theta_1 + \theta_2)$. The masses m_1 and m_2 are the point masses of the ankle and the hip respectively. l_1 is the length of link 1 that starts from the ankle joint and ends at the hip joint. l_g1 and l_g2 are the positions of m_1 and m_2 respectively.

B. Thesis Contribution

The previous work of researchers implemented different fall avoidance strategies on humanoids. They also developed a decision surface to determine when these strategies are sufficient. The disadvantage of the decision surface is that it is limited to perturbations in the sagittal and coronal planes. Our work deals with the generalization of the decision surface to a *decision volume*, used for the prediction of limiting states for recovery from disturbances in any orientation. A second contribution is the extension of the ankle and hip strategies for humanoid fall avoidance to

disturbances in random directions. The model used for the ankle strategy is a 3D Linear Inverted Pendulum Model (LIPM), whereas for the hip strategy a sphere is added to simulate the effect of the hips. Both, strategies and decision volumes are tested on the Webots simulator then implemented on a real NAO humanoid robot.

CHAPTER IV

ANKLE AND HIP STRATEGIES

This chapter presents the requirements to ensure successful fall avoidance, which could not succeed without answering the following questions:

- Is the robot going through an unstable phase that may cause a fall?

- Which fall avoidance strategy is suitable?

- What are the limitations of these strategies?

The first question is answered in Chapter II, where the concept of instability is defined: the robot's foot loses partially or completely contact with the ground and fails to return to its equilibrium position. In other words, the robot should remain within a bounded region and its velocity should not exceed a certain threshold value. These threshold values are the raw material to construct the decision volume.

The decision volume is an extension of the decision surface and its objective is to draw on a 3D plot the limiting state conditions, which are the position and velocity of the robot CoM. Given the robot's initial velocity and position, the stability of our system can now be evaluated in the more general case of random disturbances. What is observed is that the decision volume is solely determined by the robot's geometry, maximum hip torque and mass, but not a function of time.

A. Decision Volumes

1. Ankle Strategy

The ankle strategy is the default strategy used by humans to keep their balance [6] and is usually used to handle small perturbations. In order to develop the ankle strategy the robot must be first dynamically modeled. Several authors have suggested methods for modeling and controlling humanoid robots in 3D. Kajita *et al.* [21] introduced the 3D Linear Inverted Pendulum Model (3D-LIPM) to generate walking patterns for humanoids. The advantage of using this pendulum (Fig. 10) is that it can rotate around both the x-axis and the y-axis. Hence, it can deal with motion in all directions.
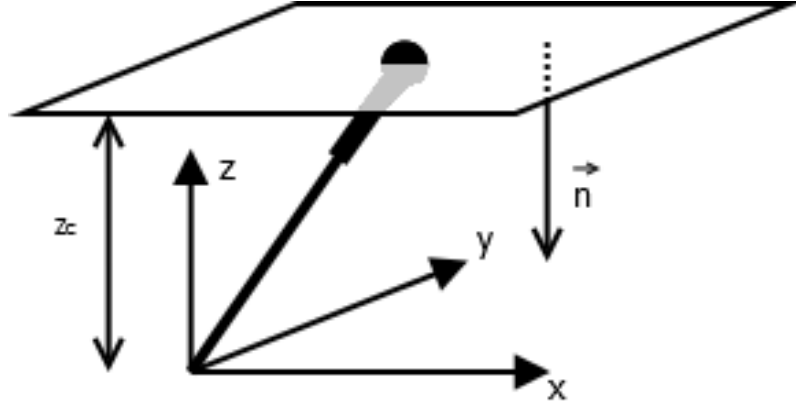

Figure 10: 3D Linear Inverted Pendulum limited to a horizontal plane

In our model, the robot's CoM is assumed to be constrained to move at a constant height $z = z_c$, along a plane parallel to the *xy*-plane. Restricting the mass movement to a horizontal plane, results in the equations of motion developed in [37, 38],

$$\ddot{x} = \frac{g}{z_c}x + \frac{1}{mz_c}\tau_y, \tag{22}$$

$$\ddot{y} = \frac{g}{z_c}y - \frac{1}{mz_c}\tau_x, \tag{23}$$

where g represents gravitational acceleration, m the pendulum's mass and τ_x, τ_y the torques across the *x*-axis and the *y*-axis respectively.

In a biped system, all joints are powered and directly controlled except the contact between the foot and the ground, which is considered as a passive joint [15]. Although this joint cannot be directly controlled, it is influenced by the dynamics of the mechanisms above the foot. The motion of the upper body has the ability to change the location of the ZMP and create a torque on the passive joint. Equations (24) and (25) present the relation between the position of the ZMP and its equivalent torques. The further away the ZMP is located, the greater the value of its torque. However, the value of the ZMP cannot exceed the support polygon. As a result, an additional limitation emerges from this relation. The maximum torques are no longer determined by the mechanical properties of the motor alone, but also by the dynamic properties of the system. Exceeding this limitation causes the robot to partially lose contact with the ground. This limitation is the basis of our decision volume.

$$p_x = \frac{-\tau_y}{mg},$$
(24)

$$p_y = \frac{\tau_x}{mg}.$$
(25)

To proceed with the development of the decision volume, (24) and (25) are rearranged for expressions in τ_y and τ_x, which are then substituted into (22) and (23) and the results are,

$$\ddot{x} = \frac{g}{z_c}(x - p_x),$$
(26)

$$\ddot{y} = \frac{g}{z_c}(y - p_y).$$
(27)

These equation are similar to the equations of the cart-table model (10) and (11), previously discussed. By subbing $x = r\cos\alpha$, $y = r\sin\alpha$, $p_x = p_r\cos\alpha$ and $p_y = p_r\sin\alpha$ into (26) and (27) and taking the sum of their squares results in

$$\ddot{r} = \frac{g}{z_c}(r - p_r).$$
(28)

The angle α determines the line of action shown in Fig. 11 as the r-axis. The value of α is independent of time. It is determined based on the direction of the push and the initial velocity vector ($\dot{\vec{r}}_0$). To cover all points in the xy-plane, $\alpha \in \left[-\frac{\pi}{2}; \frac{\pi}{2}\right]$ and $r \in \left]-\infty; \infty\right[$. When a robot is pushed, it is given an initial velocity $\dot{r}_0$ along the r-axis. To decelerate, the difference between the CoM (r) and ZMP (p_r) must be negative. Fig. 11 shows how the ZMP affects the pendulum. The torque generated by the ZMP is replaced by its equivalent force F. Since the location of the ZMP is limited to the support polygon, the equivalent recovery force F is also limited. This shows the importance of the ZMP constraint.
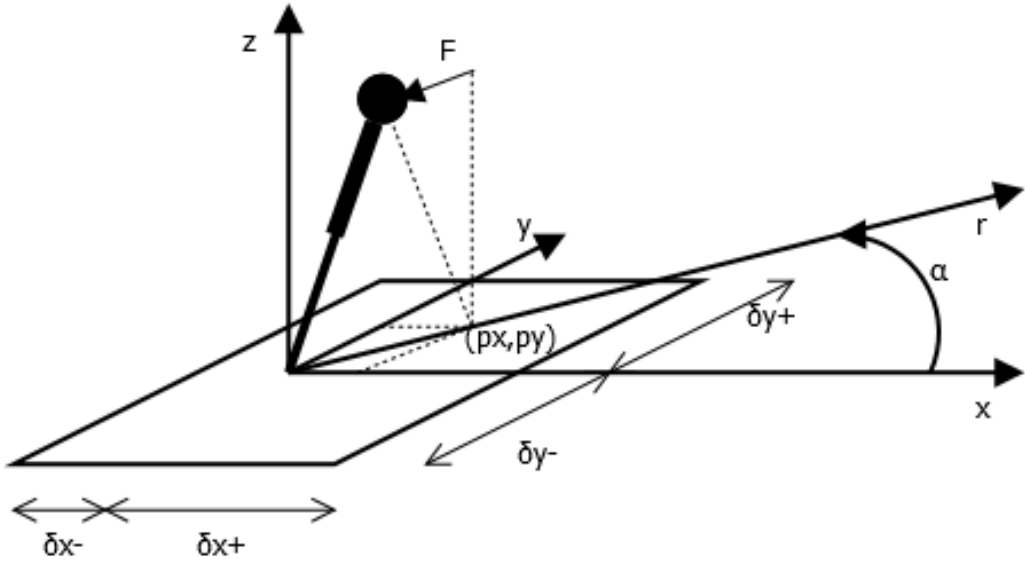

Figure 11: ZMP for the 3D-LIPM

In order to find the ankle decision volume, (28) needs to be solved. This is possible by taking the Laplace transform and solving for $R(s)$,

$$(s^2 - \omega^2)R(s) - sr_0 - s\dot{r}_0 = \omega^2 R(s) - \omega^2 \frac{p_r}{s}, \tag{29}$$

$$R(s) = \frac{s}{(s^2 - \omega^2)}r_0 + \frac{1}{(s^2 - \omega^2)}\dot{r}_0 - \frac{\omega^2}{s(s^2 - \omega^2)}p_r. \tag{30}$$

After that, taking Laplace inverse of (30), the system response $r(t)$ is found,

$$r(t) = \frac{1}{2}(r_0 + \frac{\dot{r}_0}{\omega} - p_r)e^{\omega t} + \frac{1}{2}(r_0 - \frac{\dot{r}_0}{\omega} - p_r)e^{-\omega t} + p_r, \tag{31}$$

where $\omega = \sqrt{\frac{g}{z_c}}$, r_0 and $\dot{r}_0$ represents the initial position and velocity respectively.
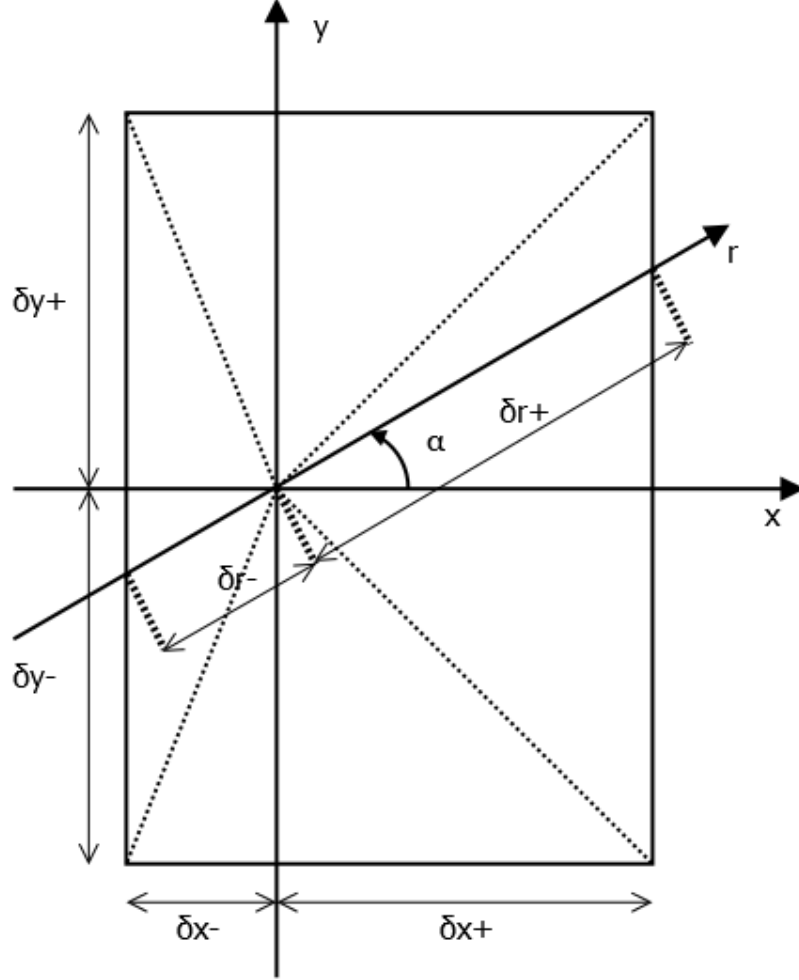

Figure 12: Support polygon

For the system to restore its stability using the ankle strategy, the coefficient of $e^{\omega t}$ in (31) must be zero. Hence, the stability condition becomes,

$$\delta_r^- < r_0 + \frac{\dot{r}_0}{\omega} < \delta_r^+, \tag{32}$$

This inequality is valid for each angle α. δ_r^+ and δ_r^- represent respectively the upper and the lower bound, shown in Fig. 12, for the ZMP across the r-axis. To find the ZMP

28

bounds the intersections between the vector r and the support polygon are calculated based on the value of α. Hence, three regions are identified for positive values of δ_r and three for negative values.

$$\delta_r^+ = \begin{cases} \frac{\delta_y^-}{\sin \alpha} & \alpha \in [-\pi/2, atan2(\delta_y^-, \delta_x^+)[\\ \frac{\delta_x^+}{\cos \alpha} & \alpha \in [atan2(\delta_y^-, \delta_x^+), atan2(\delta_y^+, \delta_x^+)[\\ \frac{\delta_y^+}{\sin \alpha} & \alpha \in [atan2(\delta_y^+, \delta_x^+), \pi/2] \end{cases} \qquad (33)$$

$$\delta_r^- = \begin{cases} \frac{\delta_y^+}{\sin \alpha} & \alpha \in [-\pi/2, atan2(\delta_y^+, \delta_x^-) - \pi[\\ \frac{\delta_x^-}{\cos \alpha} & \alpha \in [atan2(\delta_y^+, \delta_x^-) - \pi, atan2(\delta_y^-, \delta_x^-) + \pi[\\ \frac{\delta_y^-}{\sin \alpha} & \alpha \in [atan2(\delta_y^-, \delta_x^-) + \pi, \pi/2] \end{cases} \qquad (34)$$

where δ_x and δ_y represent the dimensions of the support polygon of the robot.

Based on (32), the decision volume of the ankle strategy is constructed. Fig. 13 shows the decision volume for the NAO humanoid, used in our experiments, with $z_c = 0.3m$, $\delta_x^+ = 0.105m$, $\delta_x^- = $ -0.046 m, $\delta_y^+ = 0.105m$, and $\delta_y^- = -0.105m$. An additional limit is added to the decision volume due to a geometric constraint. Since a pendulum is physically limited in length, the maximum position that CoM can reach is $r = z_c$. As a result, the decision volume becomes the region shown in Fig. 13.

The ankle decision volume shows the three states of the robot $(x_{CoM}, y_{CoM}, \dot{r}_{CoM})$. When the robot's states are within the ankle decision, the robot can rely on its ankles only to restore its balance. The red color represents the high speeds whereas, the blue color represents the low speeds.

Fig. 14 shows that for a negative value of x_{CoM} the robot can recover if its speed is positive (red color). On the other hand if x_{CoM} is positive, the robot must have a negative speed (blue color) to succeed in the recovery.

Regarding the shape of the ankle decision volume, the decision volume is symmetric along the $x - \dot{r}$-axis only. This symmetry is caused by the support polygon
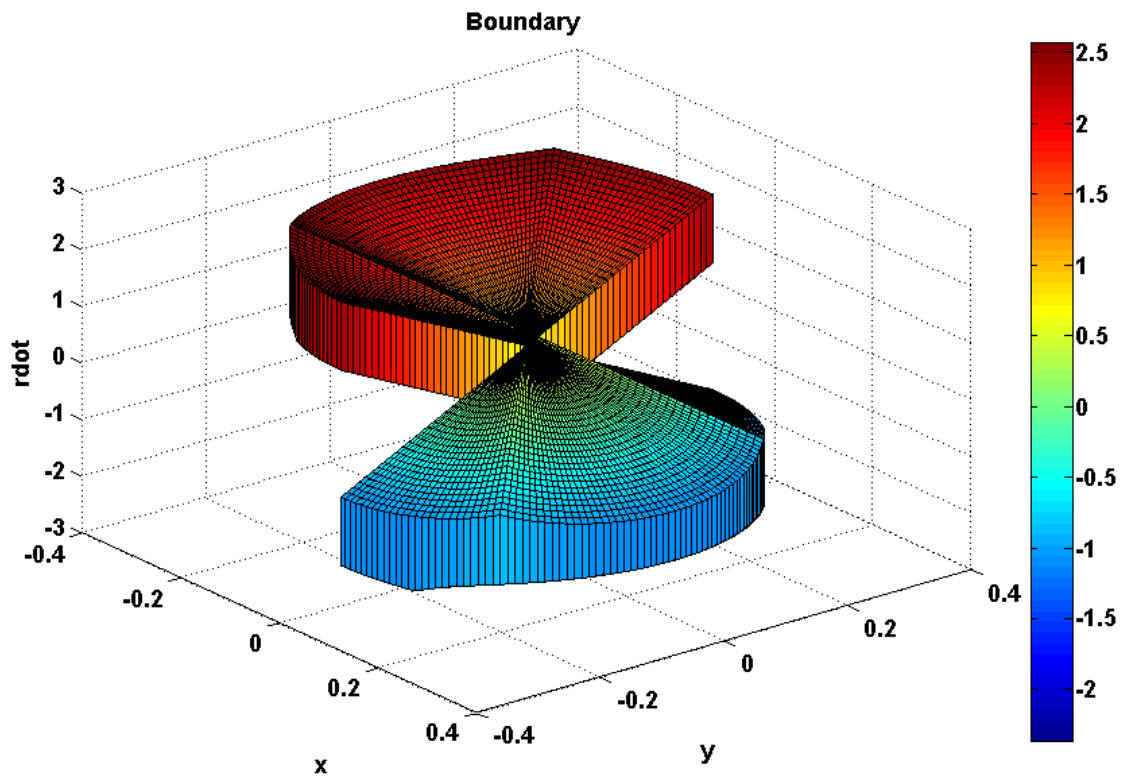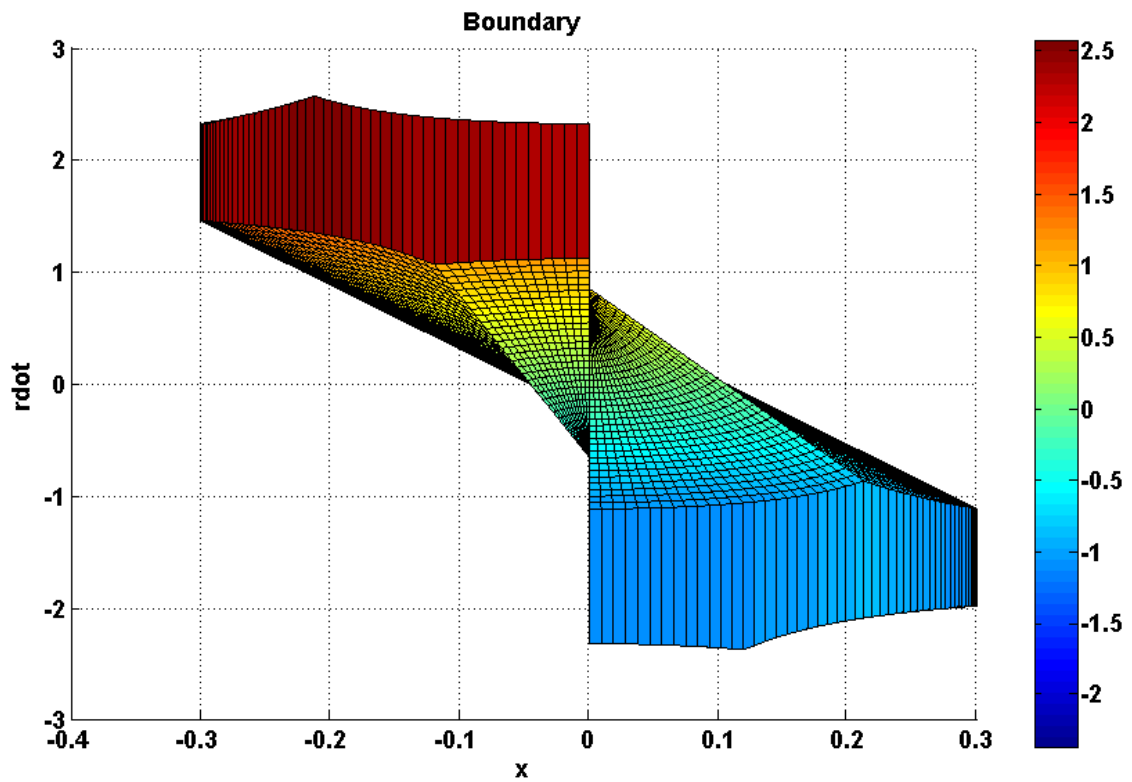
Figure 13: Decision volume for ankle strategy

Figure 14: Decision volume for ankle strategy (left view)

which is symmetric along the same axis.

For $\dot{r} = 0$ the cross section of the decision volume has the same dimensions of the support polygon. This is expected because the CoM can reach any point above the support polygon with a zero velocity and remain stable.

All lines passes through the point $x_{CoM} = 0$ and $y_{CoM} = 0$ but at different levels. This is expected because at the equilibrium point the robot can have different value of initial velocities $\dot{r}$ for different angle α.
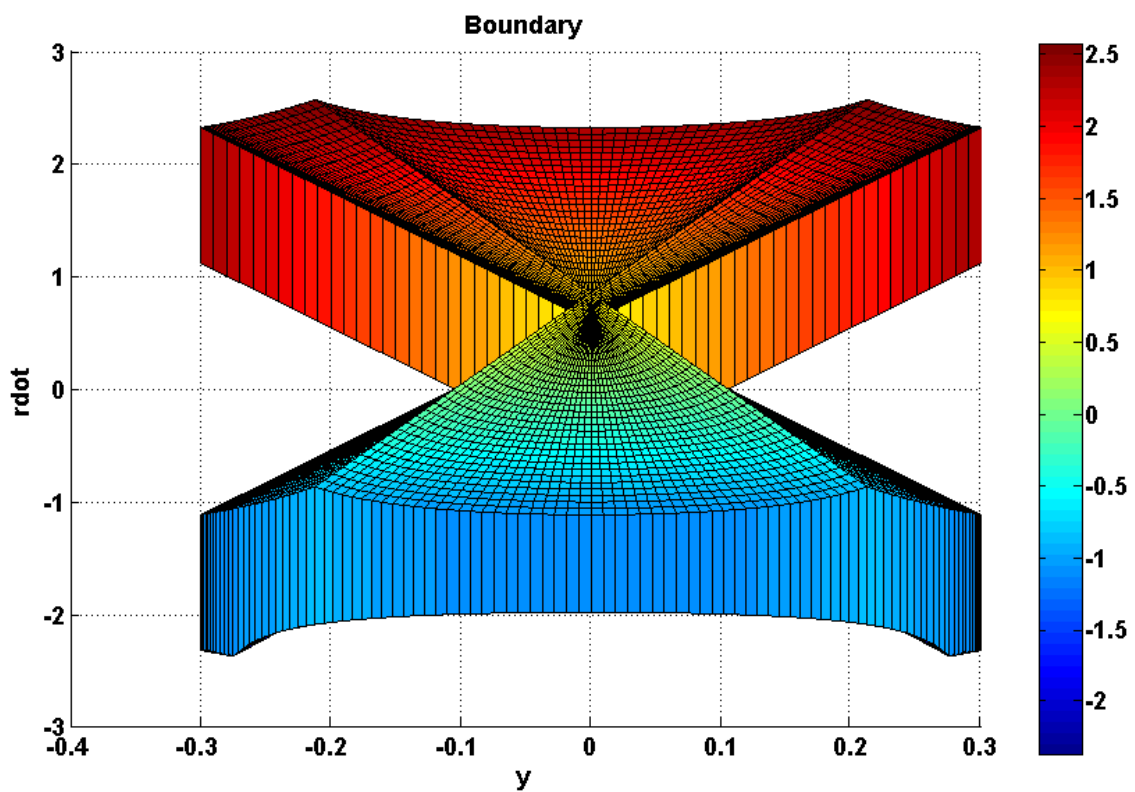

Figure 15: Decision volume for ankle strategy (front view)

2. *Hip Strategy*

Although this strategy is called the hip strategy, both ankles and hips are involved in the balance recovery. Since the hip joint is involved, the simple 3D linear inverted pendulum model with a point mass is no longer adequate to model the hip

31

strategy. As mentioned in the literature, Pratt *et al.* [25, 39], represented the effect of the hip joint by an Angular Momentum Pendulum Model (AMPM). They replaced the point mass in the inverted pendulum by a rotating disc in order to introduce the effect of the hip's momentum. For our model, since we are working in 2D rather than 1D, the point mass is replaced by a sphere (Fig. 16) where τ represents the torque generated when the upper torso accelerates.
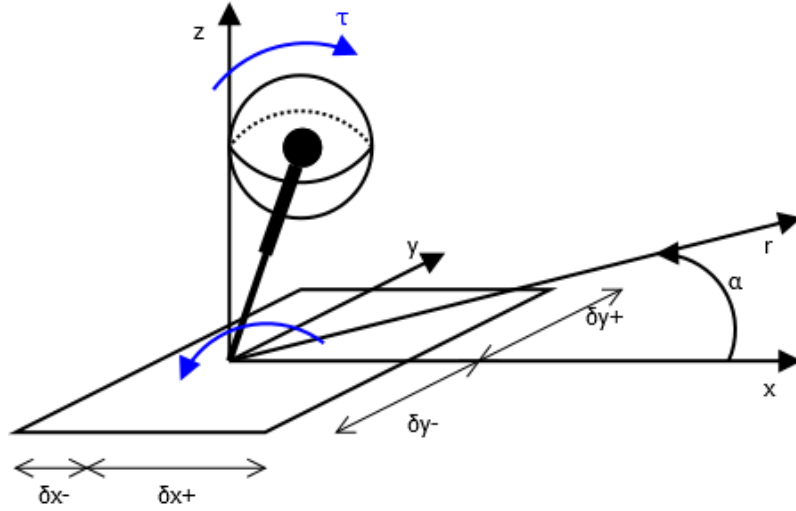

Figure 16: 3D-LIPM with the sphere to simulate the hips

As a result, our system can be expressed by the following dynamic equations:

$$\ddot{x} = \omega^2[(x - p_x) - \frac{\tau_y}{mg}], \tag{35}$$

$$\ddot{y} = \omega^2[(y - p_y) + \frac{\tau_x}{mg}]. \tag{36}$$

Equations (35) and (36) are reduced to one equation by taking the square of each one and summing them.

$$\ddot{r} = \omega^2[(r - p_r) - \frac{\tau_r}{mg}], \tag{37}$$

with,

$$\tau_x = \tau_r \cos(\pi/2 + \alpha) = -\tau_r \sin\alpha, \tag{38}$$

$$\tau_y = \tau_r \sin(\pi/2 + \alpha) = \tau_r \cos\alpha. \tag{39}$$

32

τ_x and τy shown in Fig. 17 are the roll and the pitch hip torque respectively. τ_r is the torque perpendicular to the rz-plane. The positive direction of τ_r is obtained by applying the right hand rule to the z-axis and the r-axis. Whereas τ_x and τy are the projection of τ_r ont the x and y-axis.
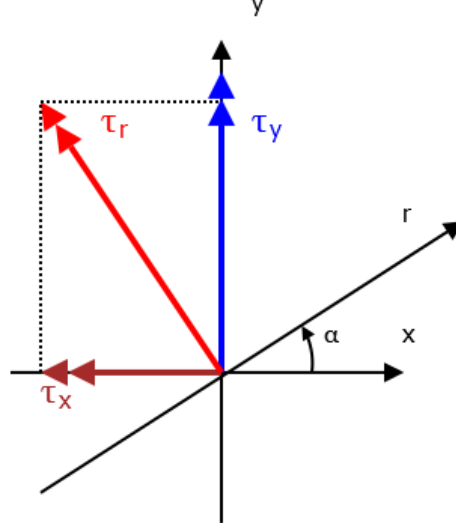

Figure 17: Hip torque directions

By examining (37), an additional term τ_r is introduced to (28) as an input. When the torso is accelerated, it reduces $\ddot{r}$ term and causes a deceleration. Although this term expands the ankle's decision volume, it will impose additional limits. The first limit is the maximum hip torque τ_{rmax}, and the second is its maximum angular position ϕ_{rmax}. Since the hip cannot accelerate indefinitely, it has to accelerate and then decelerate in time to stop before breaching the angular position constraint. At a large disturbance, the hip strategy is fully exploited. In this case, the hips are fully accelerated and decelerated using the maximum value of torque as shown in Fig. 18.

The torque equation becomes

$$\tau_r = \tau_{rmax}u(t) - 2\tau_{rmax}u(t-t_1) + \tau_{rmax}u(t-t_2), \tag{40}$$

where $u(t-\zeta)$ is a step function starting at ζ. From zero to t_1 the robot accelerates, whereas from t_1 to $t_2 = 2t_1$ it decelerates until it stops at $\phi = \phi_{rmax}$. In that case, the
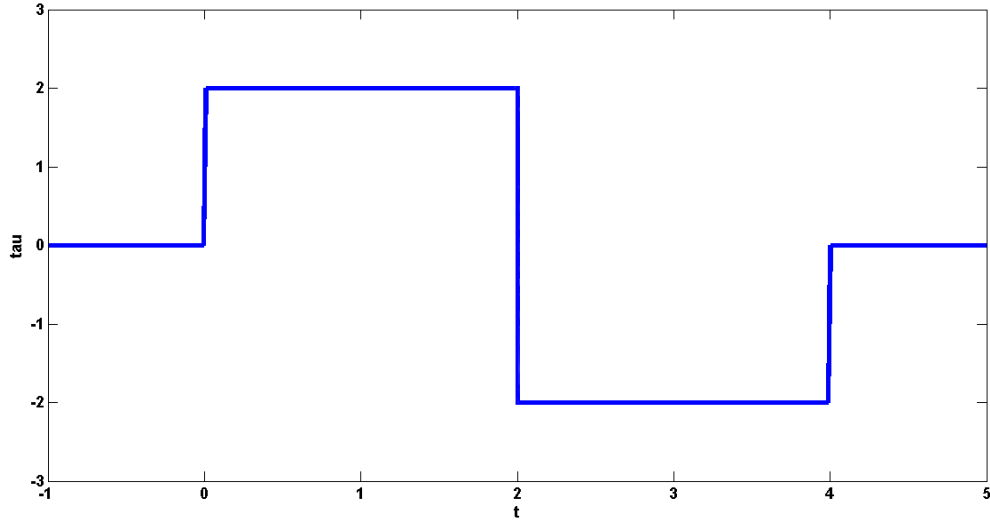
Figure 18: Torque step function

torque has the following profile (40) with $T = t_1 = \sqrt{\frac{\phi I}{\tau}}$. After the hip strategy is applied, to be successful, our system must be within the ankle decision volume (32).

Solving (37)

$$r(t) = p_r + (r_0 - p_r)\cosh(\omega t) + \frac{\dot{r}_0}{\omega}\sinh(\omega t) + \frac{(\tau_{rmax} - \tau_{rmax}\cosh(\omega t))}{mg}u(t)$$
$$+ \frac{2\tau_{rmax}[\cosh(\omega(t - t_1)) - 1]u(t - t_1) - \tau_{rmax}[\cosh(\omega(t - t_2)) - 1]u(t - t_2)}{mg}, \quad (41)$$

and then differentiating(41),

$$\dot{r}(t) = (r_0 - p_r)\omega\sinh(\omega t) + \dot{r}_0\cosh(\omega t) + \frac{-\tau_{rmax}\omega\sinh(\omega t)}{mg}u(t)$$
$$+ \frac{2\tau_{rmax}\omega[\sinh(\omega(t - t_1))]u(t - t_1) - \tau_{rmax}\omega[\sinh(\omega(t - t_2))]u(t - t_2)}{mg}. \quad (42)$$

After that for $t = 2T$ in (41) and(42),

$$r(2T) = p_r + (r_0 - p_r)\cosh(2\omega T) + \frac{\dot{r}_0}{\omega}\sinh(2\omega T) - \frac{\tau_{rmax}}{mg}[1 - 2\cosh(\omega T) + \cosh(2\omega T)], (43)$$

$$\dot{r}(2T) = (r_0 - p_r)\omega\sinh(2\omega T) + \dot{r}_0\cosh(2\omega T) - \frac{\tau_{rmax}}{mg}\omega[-2\sinh(\omega T) + \sinh(2\omega T)]. (44)$$

34

Inserting (43) and (44) in to inequality (32),

$$\left(r_0 - \delta_r^+ + \frac{\dot{r}_0}{\omega} - \frac{\tau_{rmax}}{mg}\right)e^{2\omega T} + \frac{2\tau_{rmax}}{mg}e^{\omega T} - \frac{\tau_{rmax}}{mg} < 0 \tag{45}$$

$$\left(r_0 - \delta_r^- + \frac{\dot{r}_0}{\omega} + \frac{\tau_{rmax}}{mg}\right)e^{2\omega T} - \frac{2\tau_{rmax}}{mg}e^{\omega T} + \frac{\tau_{rmax}}{mg} > 0 \tag{46}$$

Considering the worst case where the robot must execute a full hip strategy, the time needed becomes $T = T_{rmax}$

$$\delta_r^- - \frac{\tau_{rmax}}{mg}\left(e^{-\omega T_{max}} - 1\right)^2 < r_0 + \frac{\dot{r}_0}{\omega} < \delta_r^+ + \frac{\tau_{rmax}}{mg}\left(e^{-\omega T_{max}} - 1\right)^2. \tag{47}$$

Similarly to (32), the inequality in (47) is valid for every angle α. For that reason, it exists different values for τ_{rmax}. The value of τ_{rmax} varies in function of α as follows,

$$\tau_{rmax} = \begin{cases} -\frac{\tau_{xmax}}{\sin\alpha} & \alpha \in [-\pi/2, atan2(-\tau_{ymax}, \tau_{xmax})[\\[2mm] \frac{\tau_{ymax}}{\cos\alpha} & \alpha \in [atan2(-\tau_{ymax}, \tau_{xmax}), atan2(\tau_{ymax}, \tau_{xmax})[\\[2mm] \frac{\tau_{xmax}}{\sin\alpha} & \alpha \in [atan2(\tau_{ymax}, \tau_{xmax}), \pi/2] \end{cases} \tag{48}$$

Table 2 shows additional required parameters to plot the hip decision volume. τ_{xmax} (roll) and τ_{ymax} (pitch) are the values of the NAO robot motor. Roll and pitch torques are used to compute torque in each r-direction using (48). Fig. 19 shows the hip decision volume enclosing the ankle decision volume previously shown in Fig. 13. Fig. 19 also shows that the surfaces of the hip decision volume are not parallel to those of the ankle decision volume. This is caused by the additional terms that are added and vary with the line of action (r). To conclude, the hip decision volume is larger than the

Table 2: Decision volume parameters for hip strategy

τ_{xmax} (roll)	3.241 N.m
τ_{ymax} (pitch)	2.107 N.m
ϕ_{rmax}	$\pi/2$
I	$0.2\ Kg.m^2$

ankle decision volume. This means that the hip strategy can handle larger perturbation. However, the hip strategy consumes more energy because a larger number of motors are involved. The upper and lower surfaces of the hip decision volume are not parallel to that of the ankle decision volume. The hip decision volume possess the same $x\dot{r}$-plane symmetry.
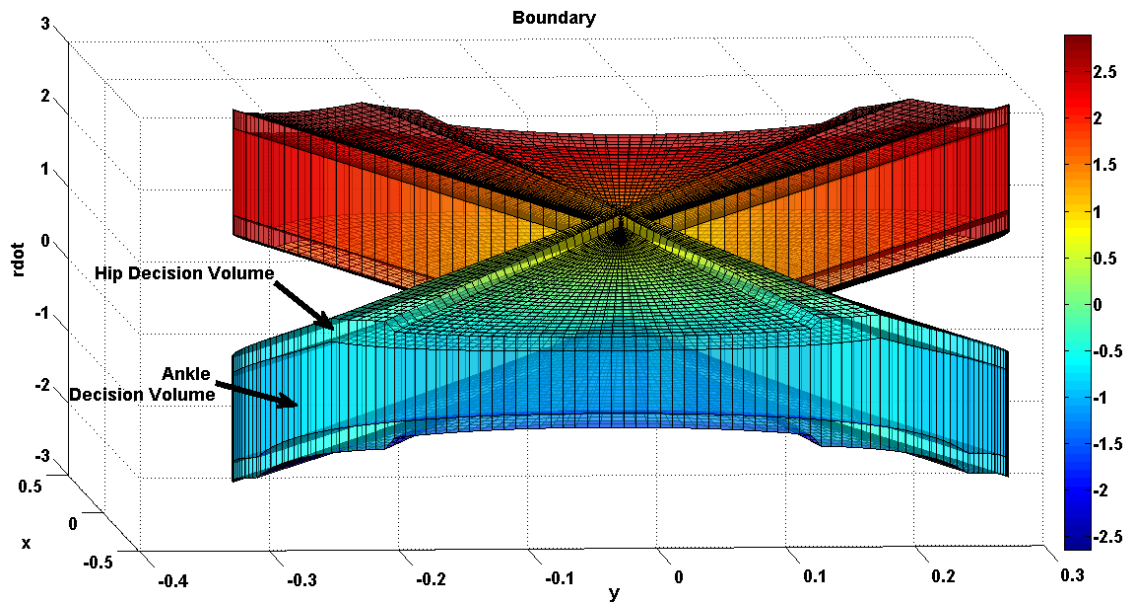

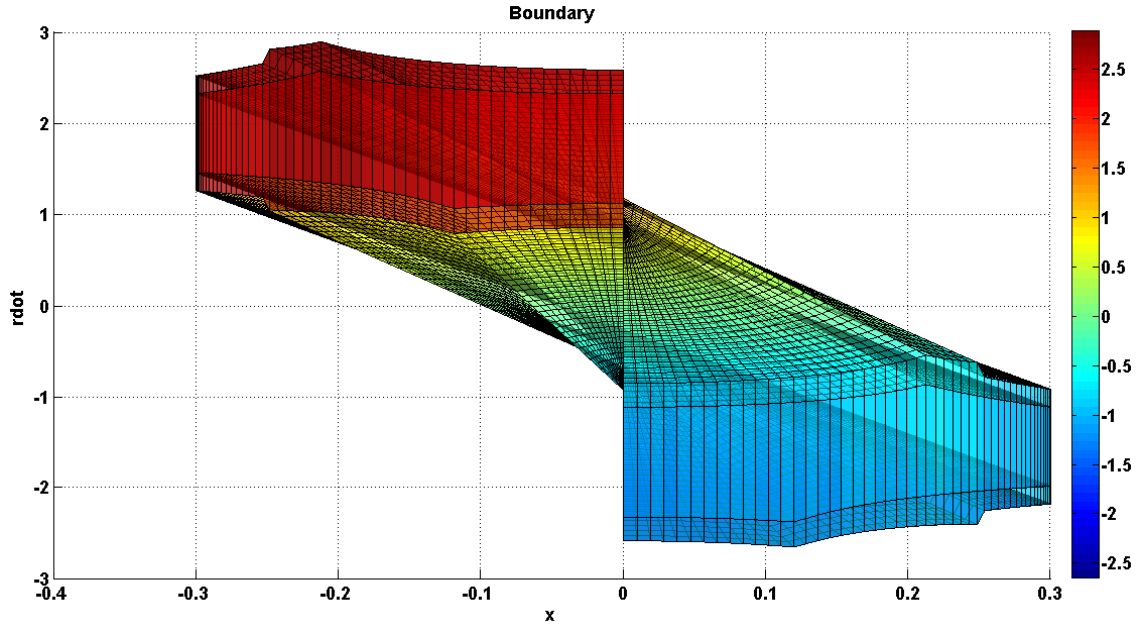Figure 19: The decision volume of the hip strategy enclosing the ankle decision volume

Figure 20: The decision volume of the hip strategy enclosing the ankle decision volume (left view)

B. Control

To proceed with the control, the simplified models developed before are not sufficient. Instead, a more realistic version is considered. In this version the system is made of 8 DoF, distributed as mentioned in chapter II. Nevertheless, this number can be reduced to 4 when only one foot is in contact with the ground. Although the robot starts with both feet on the ground, one of them may lose contact. For that reason, there are two modes of operation. The first one is the double support mode, where both of the feet are on the ground, whereas the second mode is the single support mode, where the robot is supported by one foot. In the first mode, the support polygon is larger and both of the legs can be used for balance recovery. In the second mode although the support polygon is reduced to one foot, the parameters of the initial support polygon are still valid. The reason for that is that the robot will replace its second foot. In this mode, only one leg is used to apply the strategies.

In the next sections, the VMC is used to develop the ankle and the hip strategies. Virtual springs and dampers are added then their effects are transferred to the motors.

1. Ankle Strategy (VMC)

Pratt *et al.* [8] applied this framework to a physical planar bipedal robot. Using this control strategy, they implemented a walking pattern to the Spring Flamingo robot and the Spring Turkey robot. Jalgha *et al.*[31, 32] used the VMC method in their fall avoidance strategies. The VMC is based on placing virtual mechanical components such as springs and dampers. After that, the forces and moments required to actuate a robot's motors are computed. For the model in this thesis, a spring and a damper are attached to the CoM along each of the *x*-axis and the *y*-axis as shown in Fig. 21.
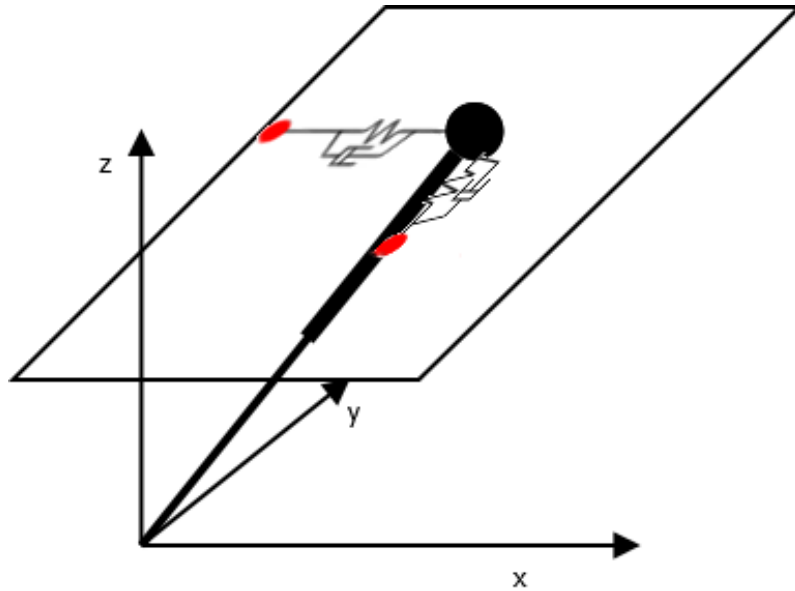

Figure 21: VMC for ankle strategy

The resultant forces of the virtual springs and dampers are shown in Fig. 22,

$$F_x = -K_x x - B_x \dot{x}, \tag{49}$$

$$F_y = -K_y y - B_y \dot{y}. \tag{50}$$

K and *B* represent the springs and dampers constants. $F_z = mg$ is the force required to compensate for the weight.

Since these components are virtual, their desired effects are applied to the
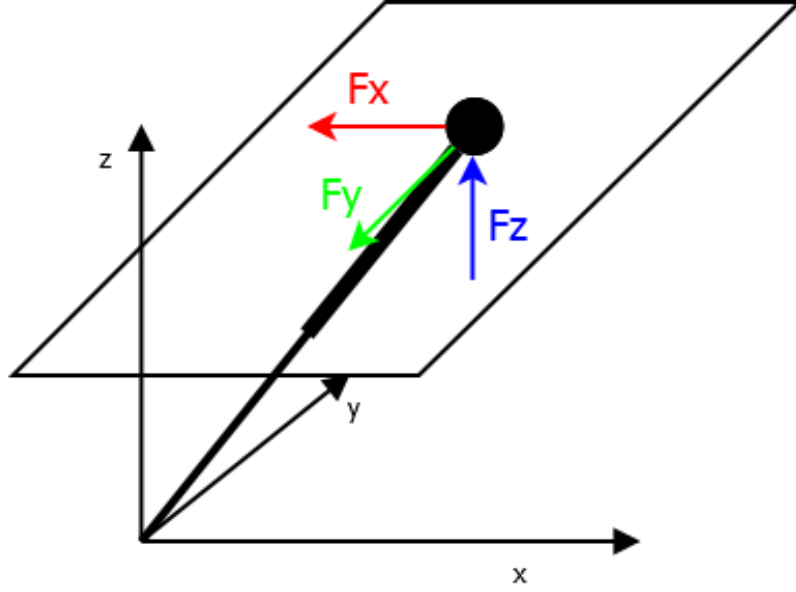
Figure 22: VMC forces for ankle strategy

pendulum via the roll and pitch ankle motor torques as follows:

$$\tau_x = F_y z_c + mgy, \tag{51}$$

$$\tau_y = F_x z_c - mgx. \tag{52}$$

For the real robot, the forces are applied in a more complicated manner. Before applying these torques, the Jacobian matrix must be computed in order to relate the virtual forces to the robots motors. In what follows, the left leg is assumed to maintain contact with the ground. The same calculation can be done in the case of the right leg. To compute the Jacobian matrix, first of all, the location of the CoM is calculated,

$$\begin{bmatrix} x \\ y \\ z \end{bmatrix} = \begin{bmatrix} \sin(a_{Lpitch})(L_{torso}\cos(a_{Lroll}) + L_{ah}\cos(a_{Lroll}) - L_{wa}\sin(a_{Lroll})) \\ L_{wa} - L_{wa}\cos(a_{Lroll}) - L_{torso}\sin(a_{Lroll}) - L_{ah}\sin(a_{Lroll}) \\ \cos(a_{Lpitch})(L_{torso}\cos(a_{Lroll}) + L_{ah}\cos(a_{Lroll}) - L_{wa}\sin(a_{Lroll})) \end{bmatrix}. \tag{53}$$

Then the following derivatives are calculated to find the Jacobian.

$$\mathbf{J} = \begin{bmatrix} \dfrac{\partial x}{\partial a_{Lpitch}} & \dfrac{\partial x}{\partial a_{Lroll}} \\[2ex] \dfrac{\partial y}{\partial a_{Lpitch}} & \dfrac{\partial y}{\partial a_{Lroll}} \\[2ex] \dfrac{\partial z}{\partial a_{Lpitch}} & \dfrac{\partial z}{\partial a_{Lroll}} \end{bmatrix} \tag{54}$$

$$\begin{aligned} \frac{\partial x}{\partial a_{Lpitch}} &= cos(a_{Lpitch})(L_{torso}cos(a_{Lroll}) + L_{ah}cos(a_{Lroll}) - L_{wa}sin(a_{Lroll})), \\ \frac{\partial x}{\partial a_{Lroll}} &= -sin(a_{Lpitch})(L_{torso}sin(a_{Lroll}) + L_{ah}sin(a_{Lroll}) + L_{wa}cos(a_{Lroll})), \\ \frac{\partial y}{\partial a_{Lpitch}} &= 0, \\ \frac{\partial y}{\partial a_{Lroll}} &= L_{wa}sin(a_{Lroll}) - L_{ah}cos(a_{Lroll}) - L_{torso}cos(a_{Lroll}), \\ \frac{\partial z}{\partial a_{Lpitch}} &= -sin(a_{Lpitch})(L_{torso}cos(a_{Lroll}) + L_{ah}cos(a_{Lroll}) - L_{wa}sin(a_{Lroll})), \\ \frac{\partial z}{\partial a_{Lroll}} &= -cos(a_{Lpitch})(L_{torso}sin(a_{Lroll}) + L_{ah}sin(a_{Lroll}) + L_{wa}cos(a_{Lroll})). \end{aligned} \tag{55}$$

Finally, the transpose of the Jacobian is multiplied by the desired forces in order to find the ankle torques.

$$\begin{bmatrix} \tau_{a_{Lpitch}} \\[1ex] \tau_{a_{Lroll}} \end{bmatrix} = \mathbf{J^T} \begin{bmatrix} F_x \\ F_y \\ F_z \end{bmatrix} \tag{56}$$

The effect of these torques makes the robot acts as if it was connected to the virtual springs and dampers shown in Fig. 21. This allows the robot to recover using only its ankles.

2. Hip Strategy (VMC)

The hip strategy is built on top of the ankle strategy. For this strategy there is two additional DoF, these are the hips roll and pitch motors. These motors must accelerate in the same direction of the fall in order to avoid it. Regarding the ankles, they are actuated in the same manner explained in the previous section. This means that the

40

same virtual forces are used to compute the ankles torque.
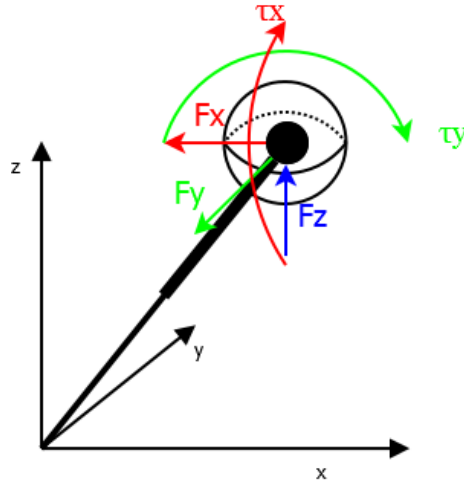

Figure 23: Forces and moments for hip strategy

A Proportional-Derivative (PD) controller is used to control the hips. The sphere's torques should be proportional to the CoM position and the CoM velocity. The greater the distance between the equilibrium position and CoM is, the larger the torque. Also, the greater the velocity of the CoM is, the larger the torque. Finally, the motion of the sphere is damped with respect to its angular velocity. This results in the following equations,

$$\tau_{Hpitch} = K_{Hpitch}x + B_{Hpitch}\dot{x} - V_{Hpitch}\dot{\phi}_{pitch}, \tag{57}$$

$$\tau_{Hroll} = K_{Hroll}y + B_{Hroll}\dot{y} - V_{Hroll}\dot{\phi}_{roll}. \tag{58}$$

K, B and V are the control parameters.

Although these torques are applied on the sphere model, they are not exactly the same for the realistic model. In the real model, the CoM is not on the hip level.

Therefore, to apply the hip strategy, the Jacobian is again computed.

$$
\begin{bmatrix} x \\ y \\ z \\ Pitch \\ Roll \end{bmatrix} = \begin{bmatrix} x_{CoM} & (6) \\ y_{CoM} & (7) \\ z_{CoM} & (8) \\ a_{Lpitch} + h_{Lpitch} \\ a_{Lroll} + h_{Lroll} \end{bmatrix}
\tag{59}
$$

$$
\mathbf{J} = \begin{bmatrix}
\frac{\partial x}{\partial a_{Lpitch}} & \frac{\partial x}{\partial a_{Lroll}} & \frac{\partial x}{\partial h_{Lroll}} & \frac{\partial x}{\partial h_{Lpitch}} \\
\frac{\partial y}{\partial a_{Lpitch}} & \frac{\partial y}{\partial a_{Lroll}} & \frac{\partial y}{\partial h_{Lroll}} & \frac{\partial y}{\partial h_{Lpitch}} \\
\frac{\partial z}{\partial a_{Lpitch}} & \frac{\partial z}{\partial a_{Lroll}} & \frac{\partial z}{\partial h_{Lroll}} & \frac{\partial z}{\partial h_{Lpitch}} \\
\frac{\partial Pitch}{\partial a_{Lpitch}} & \frac{\partial Pitch}{\partial a_{Lroll}} & \frac{\partial Pitch}{\partial h_{Lroll}} & \frac{\partial Pitch}{\partial h_{Lpitch}} \\
\frac{\partial Roll}{\partial a_{Lpitch}} & \frac{\partial Roll}{\partial a_{Lroll}} & \frac{\partial Roll}{\partial h_{Lroll}} & \frac{\partial Roll}{\partial h_{Lpitch}}
\end{bmatrix}
\tag{60}
$$

$$
\mathbf{J^T} = \begin{bmatrix}
\frac{\partial x}{\partial a_{Lpitch}} & \frac{\partial y}{\partial a_{Lpitch}} & \frac{\partial z}{\partial a_{Lpitch}} & 1 & 0 \\
\frac{\partial x}{\partial a_{Lroll}} & \frac{\partial y}{\partial a_{Lroll}} & \frac{\partial z}{\partial a_{Lroll}} & 0 & 1 \\
\frac{\partial x}{\partial h_{Lroll}} & \frac{\partial y}{\partial h_{Lroll}} & \frac{\partial z}{\partial h_{Lroll}} & 0 & 1 \\
\frac{\partial x}{\partial h_{Lpitch}} & \frac{\partial y}{\partial h_{Lpitch}} & \frac{\partial z}{\partial h_{Lpitch}} & 1 & 0
\end{bmatrix}
\tag{61}
$$

$$
\begin{bmatrix} \tau_{a_{Lpitch}} \\ \tau_{a_{Lroll}} \\ \tau_{h_{Lroll}} \\ \tau_{h_{Lpitch}} \end{bmatrix} = \mathbf{J^T} \begin{bmatrix} F_x \\ F_y \\ F_z \\ \tau_{pitch} \\ \tau_{roll} \end{bmatrix}
\tag{62}
$$

After calculating the torques in (62), the ankles torque become,

$$
\tau_{a_{Lpitch}} = \frac{\partial x}{\partial a_{Lpitch}} F_x + \frac{\partial y}{\partial a_{Lpitch}} F_y + \frac{\partial z}{\partial a_{Lpitch}} F_z + \tau_{pitch},
\tag{63}
$$

$$
\tau_{a_{Lroll}} = \frac{\partial x}{\partial a_{Lroll}} F_x + \frac{\partial y}{\partial a_{Lroll}} F_y + \frac{\partial z}{\partial a_{Lroll}} F_z + \tau_{roll}.
\tag{64}
$$

In general, this procedure is used for the manipulators. In order for our control to succeed, the τ_{pitch} and τ_{roll} from (63) and (64) are removed. Because by keeping these torque the momentum effect of the hip joint rotation is canceled. In order to avoid that, τ_{pitch} and τ_{roll} from (63) and (64) are set to zero. Hence, the hip torque acts in the opposite direction as shown in Fig. 16.

CHAPTER V

SIMULATIONS AND RESULTS

In this chapter, the simulations and the implementations of the strategies are done, and the results are discussed. The first type of simulations is the numeric simulations, using Matlab and Simulink. Multiple initial conditions are used to validate the decision volumes. The initial conditions are mainly the initial velocity $\dot{r}_0$ and its direction, represented by angle α. The control used in these simulations is the VMC, which was previously discussed. The second type of simulations is done on Webots [9], a simulator for mobile robotics, which includes in its library the NAO robot, a replication of a realistic humanoid robot. In the second type of simulations, the robot is pushed by an external force. After succeeding in the simulations, both strategies are implemented on the real NAO robot.

A. Numerical Simulations

1. Ankle Strategy 3D-LIPM

Ankle strategy is tested on the 3D-LIPM. Fig. 24 shows the plots of different simulation. The red line is the case where $\dot{r}_0 = 0.6 m/s$ and $\alpha = \pi/4$. The green line is the case where $\dot{r}_0 = 0.6 m/s$ and $\alpha = -\pi/3$. The blue line is the case where $\dot{r}_0 = -0.5 m/s$ and $\alpha = \pi/4$. In all of the three cases the pendulum return to its initial position with zero velocity $(x = 0, y = 0, \dot{r} = 0)$. The yellow line has the following initial conditions, $\dot{r}_0 = 0.9 m/s$ and $\alpha = \pi/4$. This initial condition falls beyond the ankle decision volume. As a result, the pendulum cannot return to its initial state. In this case, the velocity profile starts at $\dot{r}_0 = 0.9 m/s$ as expected, and then it decelerates to

$\dot{r}(0.305) = 0.2984 m/s$. After that, it accelerates indefinitely. This behavior can be explained by referring to (28). In the deceleration part p_r is larger than r. Then, when p_r reaches its saturation value, which is the support polygon limit, with a positive velocity, the CoM keeps on moving to exit from the support polygon. Hence, r becomes larger than p_r. As a result, the CoM accelerates and cannot return to the support polygon. In consequence, the acceleration is indefinite.
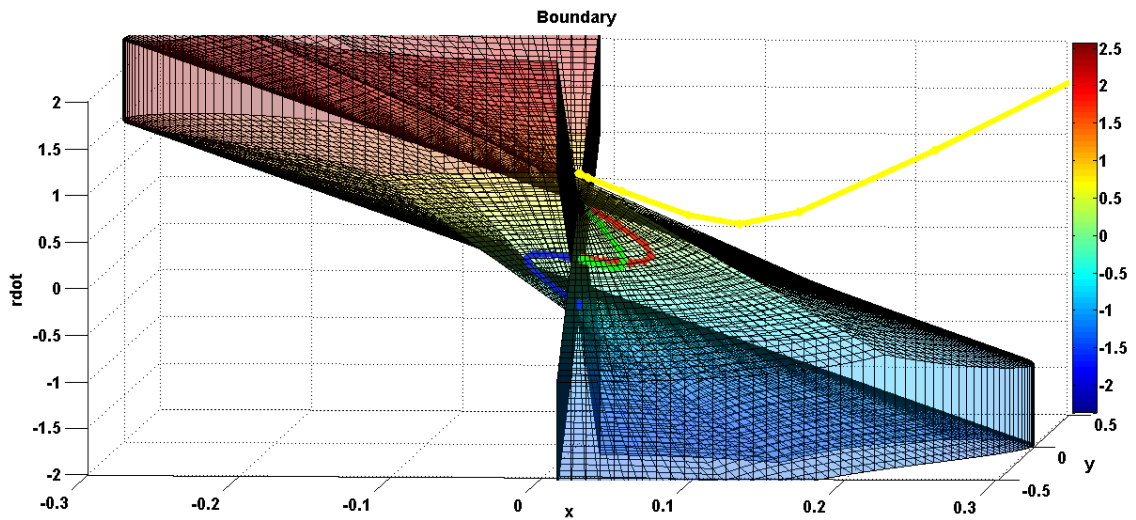
Figure 24: Decision volume for 3D-LIPM with different initial conditions (side view)
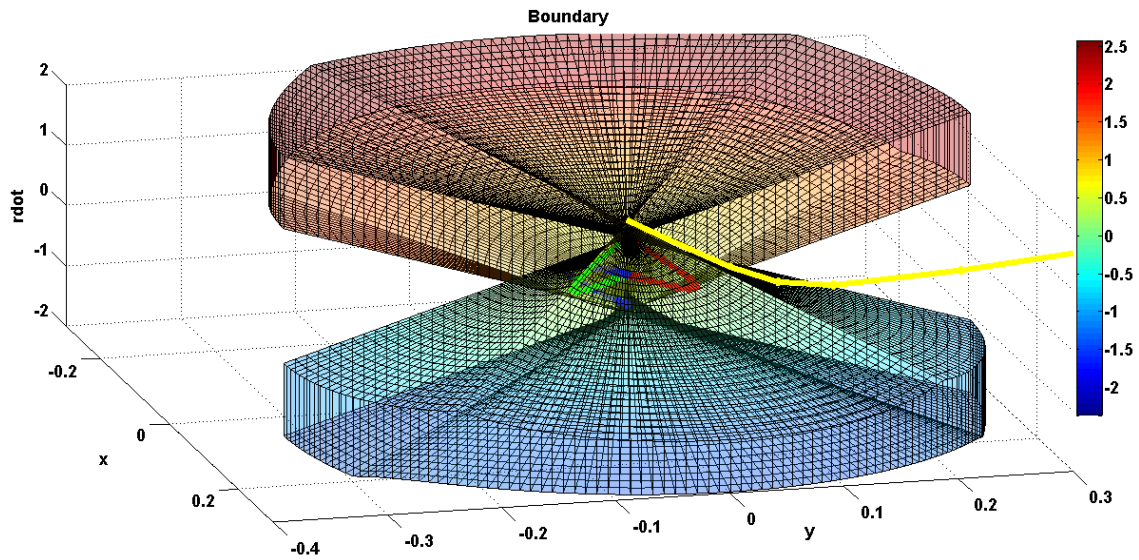

Figure 25: Decision volume for 3D-LIPM with different initial conditions

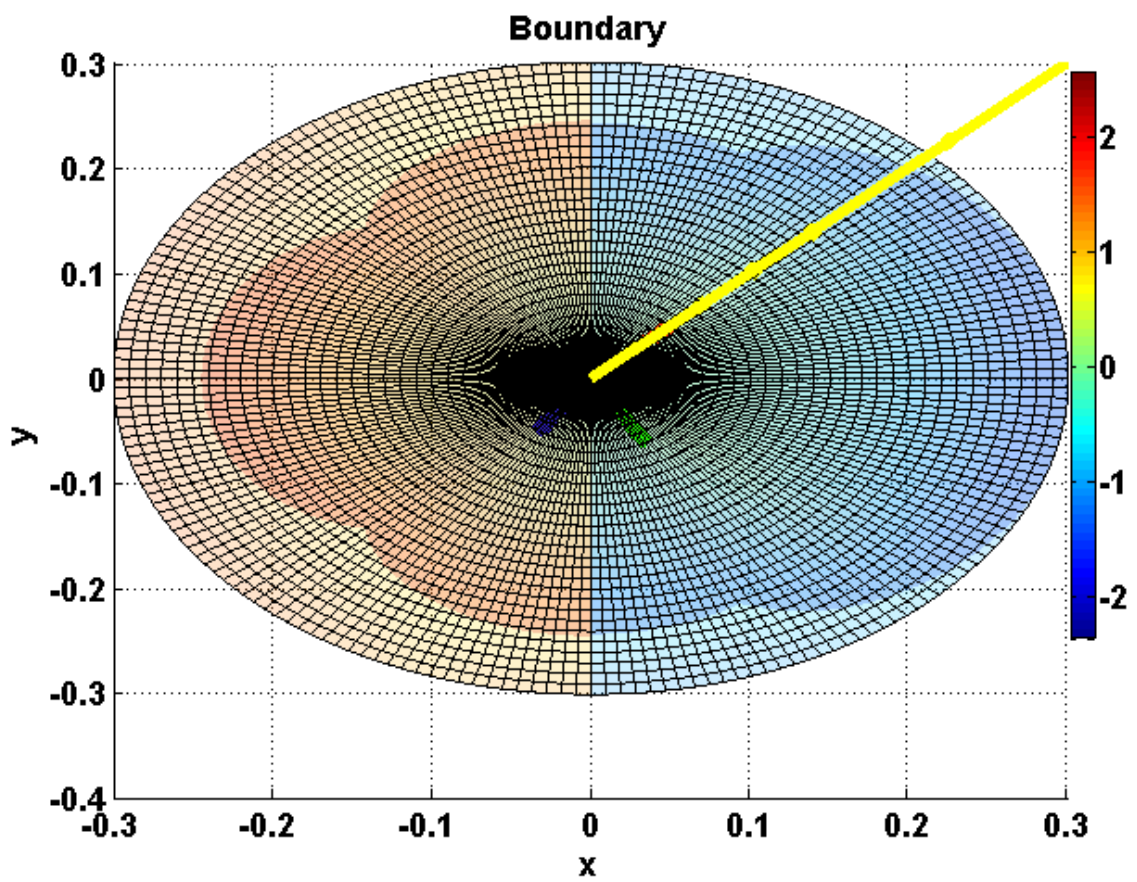Fig. 26 shows that through the simulation the CoM goes through a linear motion with a constant value of α.

45

Figure 26: Decision volume for 3D-LIPM with different initial conditions (top view)

46

Table 3 shows the parameters of the simulations.

Table 3: 3D-LIPM parameters

L	$0.3m$
m	$5Kg$
δ_x^+	$0.105m$
δ_x^-	$-0.046m$
δ_y^+	$0.105m$
δ_y^-	$-0.105m$
K_x, K_y	50
V_x, V_y	35

Fig. 27 shows the velocity profile of the previous simulation ($\dot{r}_0 = 0.6m/s$ and $\alpha = \pi/4$). The velocity starts at $0.6m/s$, which is determined by the initial condition, then decelerates to reach a value of $-0.07m/s$ then stops and reverts its direction. Finally, the system reaches its equilibrium state.
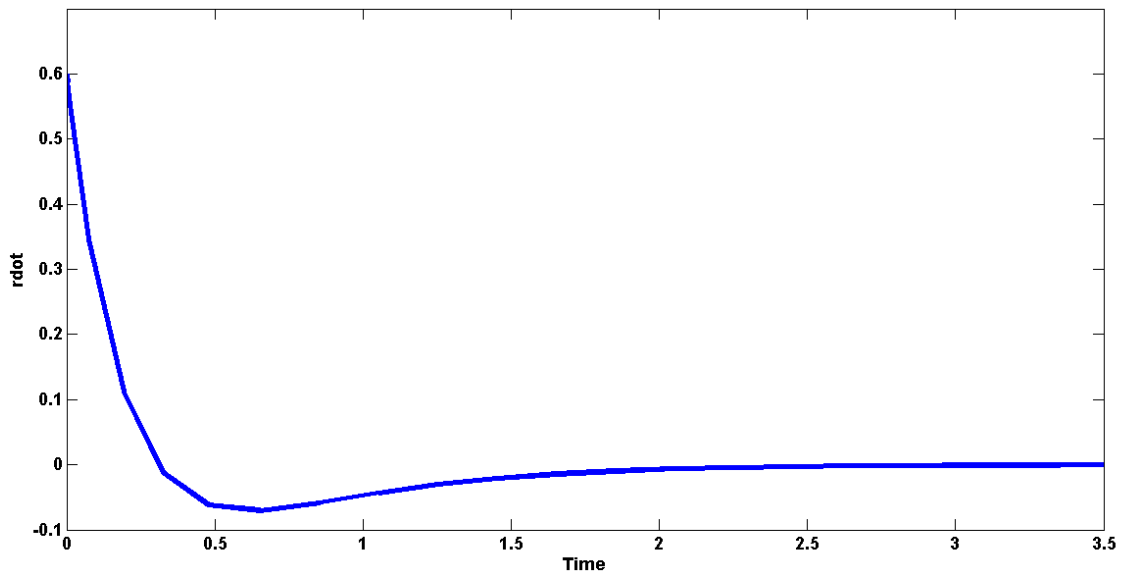

Figure 27: $\dot{r}$ vs time for $\dot{r}_0 = 0.6m/s$ and $\alpha = \pi/4$
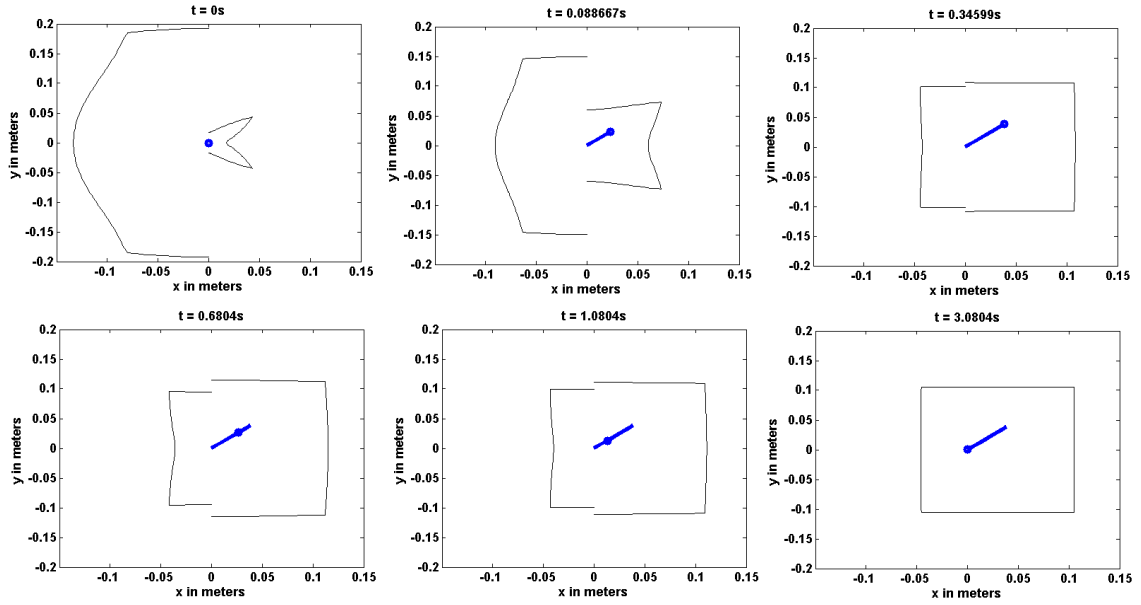
Figure 28: CoM position bounded by the decision volume contour plot for ($\dot{r}_0 = 0.6m/s$ and $\alpha = \pi/4$)

Fig. 28 shows the trajectory of the CoM in the *xy*-plane in blue, and the contour plot of the decision volume at a given velocity. This figure shows that the trajectory is a straight line which is consistent with our assumption that the angle α is constant. In addition, the first frame shows a relatively small region. Then, through time, the velocity decreases causing the region to vary accordingly. In this case, the region increases. Finally, when the velocity becomes zero, the contour plot takes the shape of the support polygon shown in the last frame.

2. Hip Strategy 3D-LIPM with Sphere

In this section, the hip simulation is done using the same parameters of the ankle simulation (Table 3). The additional parameters are required to plot the hip decision volume are $\tau_{roll} = 3.2409N.m$, $\tau_{pitch} = 2.1067N.m$, and $I = 0.18Kg.m^2$.

The next simulation is done using the same initial conditions of the yellow line in the ankle strategy ($\dot{r}_0 = 0.9m/s$ and $\alpha = \pi/4$), however in this simulation the hip

strategy is used. The results are shown in Fig. 29. In this case, the decision volume includes the whole curve. Fig. 30 shows the velocity profile of the simulation where $\dot{r}$
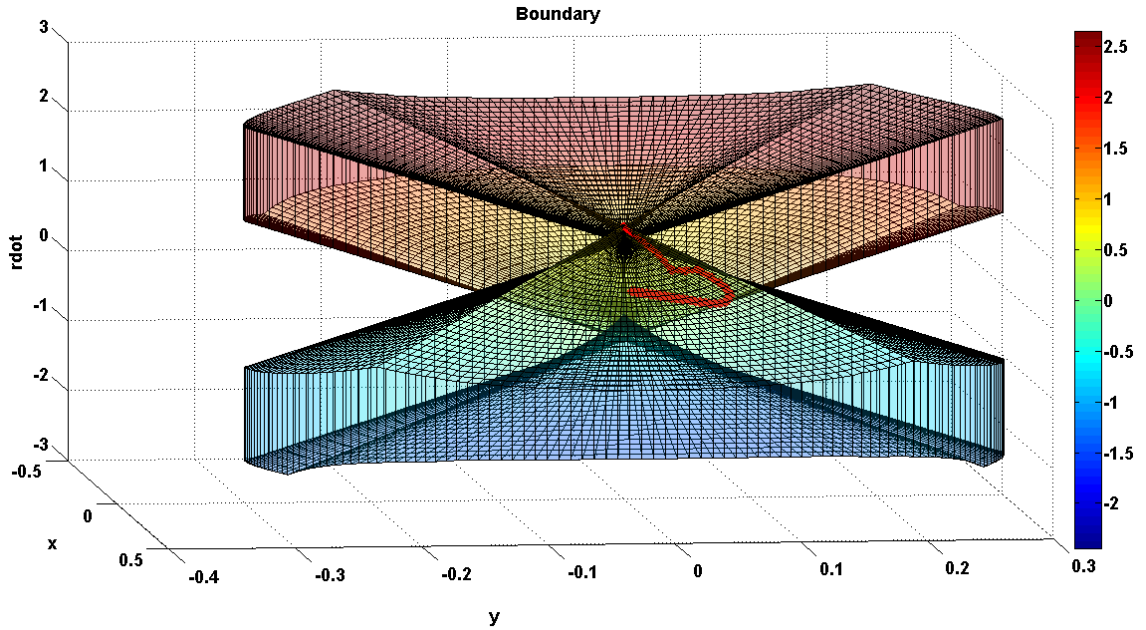

Figure 29: Hip decision volume with $\dot{r}_0 = 0.9m/s$ and $\alpha = \pi/4$

starts at $0.9m/s$ and then decelerates to $\dot{r}(0.0828) = 0.323m/s$. In this phase, the hip strategy is in the acceleration mode. Then, due to the hip deceleration, a small acceleration occurs to the CoM and its velocity reaches $0.325m/s$ at $t = 0.165s$. Finally, the hip strategy is finished, and our system moves within the decision surface of the ankle strategy. In that case, only the ankle strategy is active and is sufficient to get back to the equilibrium state.

A comparison of the two strategies shows that the hip strategy succeeds in recovering from an initial velocity of $0.9m/s$ at an angle $pi/4$, where the ankle strategy failed to do so. This fact shows the advantage of the hip strategy over the ankle strategy.
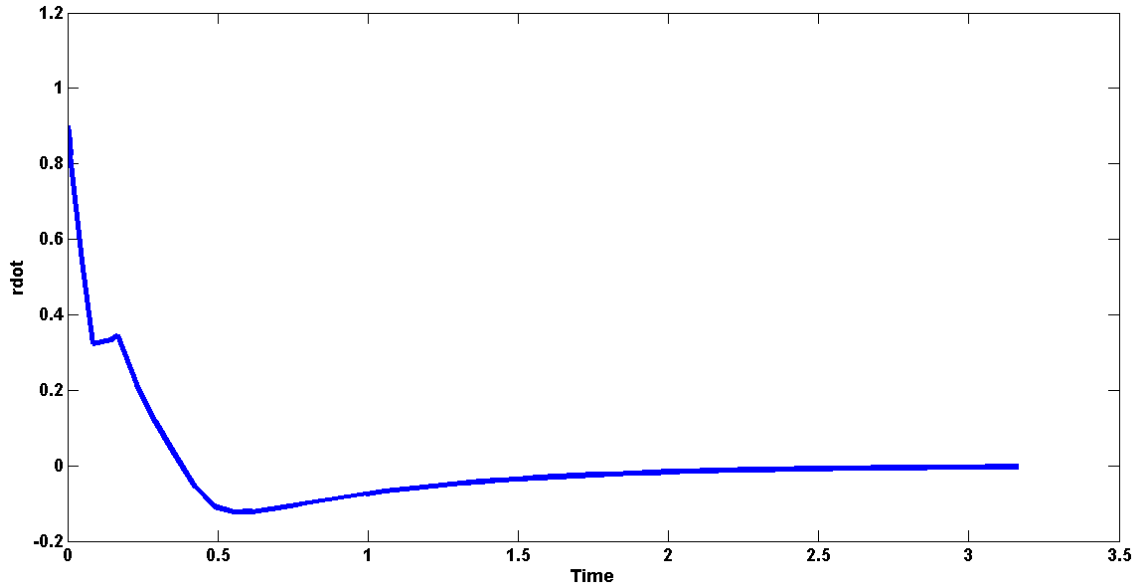
Figure 30: $\dot{r}$ plot in function of time for the hip strategy

B. Webots Simulation

In this section the simulations are done on Webots [9]. This simulator is used for mobile robots and it includes in its library many robots. For our simulation NAO (H25 V3.3), which already exists in the Webots library, is used. The push is applied by using the physics plug-in toll in the simulator. In this tool, the force vector is determined by its point of application, direction, module, and the period of application. In these simulations, the point of application at 0.4 m of height, its direction and magnitude vary with each simulation. For all the simulation, the force vector is confined in a plane parallel to the *xy*-plane. Finally the time of application of the force is set to 0.1 seconds.

1. Ankle Strategy

Fig. 31 shows snapshots of the Webots simulation done on the NAO robot. In this simulation the amplitude of the force is 30*N* and has an orientation of $\pi/4$. This figure shows the reaction of the robot. In this simulation, the robot is pushed from its right backside. The motion of the CoM propagates in the same direction of the push. In

this case, the main foot (actuated foot) that is responsible of the strategy implementation is the left foot. When pushed, the robot's right foot loses its contact with the ground. After the strategy is applied, the robot gets back to its initial position and both of its feet are in contact with the ground.
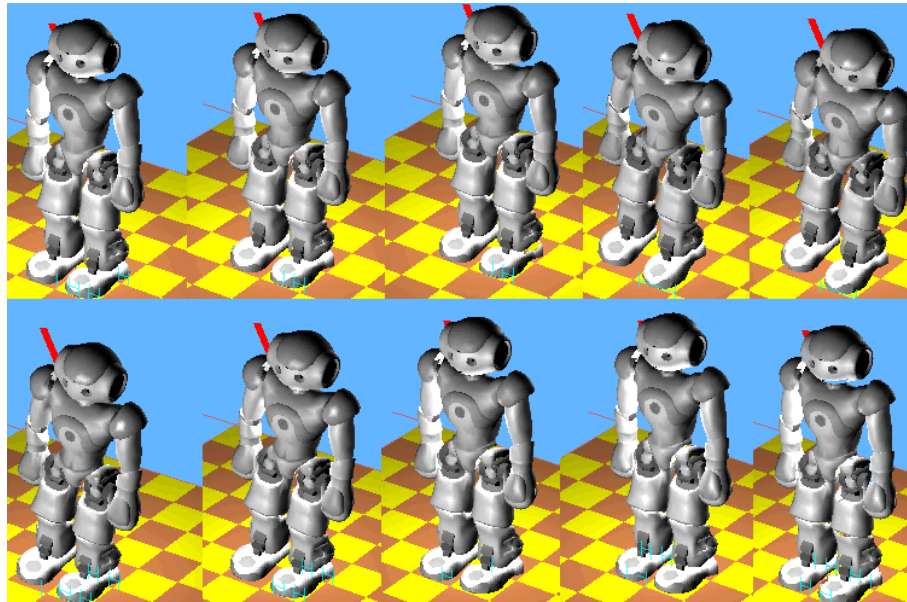

Figure 31: Webots simulation for a 30N of force at an angle $\alpha = \pi/4$

The decision volume for the Webots simulation is shown in Fig. 32. All the points that represent the three states of the robot are within the decision volume. As a result, the robot is able to restore its balance. In this simulation, the robot reaches a top speed of $0.471m/s$, then decelerates until it reaches $-0.25m/s$. After that, it bounces for a period of time till it settles at zero.

Fig. 33 shows the trajectory of the CoM of the Webots simulation. The CoM reaches a maximum of $0.041m$ along the x-axis and $0.053m$ along the y-axis. In this figure, the CoM trajectory is not a completely straight line. There is a small amount of divergence. This divergence is due to the large perturbation and the limitation of the support polygon that add some disturbances to the control. Also, the foot shape has an impact on the trajectory when the actuated foot partially loses contact with the ground.

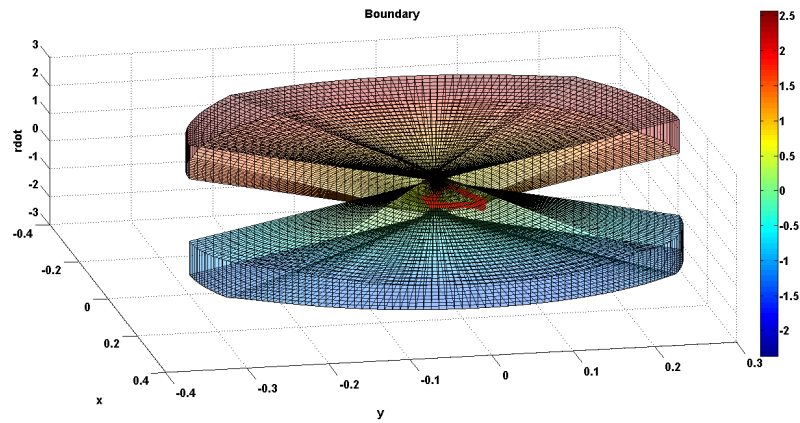Another trajectory is shown in Fig. 34. This is a result of a Webots simulation

Figure 32: Ankle decision volume for Webots simulation ($F = 30N$ and $\alpha = \pi/4$)
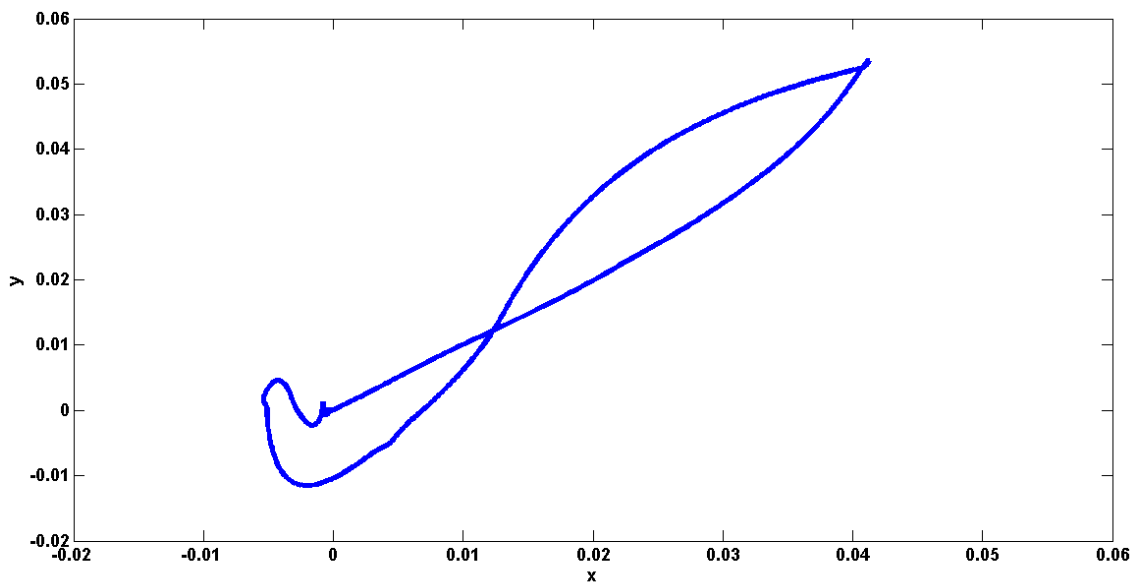

Figure 33: CoM trajectory ($F = 30N$ and $\alpha = \pi/4$)

with a 25N push instead of 30N. In this figure, the CoM starts at $(0,0)$ and moves linearly until it reaches $(0.035m, 0.035m)$, all the while keeping an angle of $\pi/2$. Beyond that point, there is no guarantee of a linear trajectory, because the VMC is applied along x and y and does not act along the same line of action r.
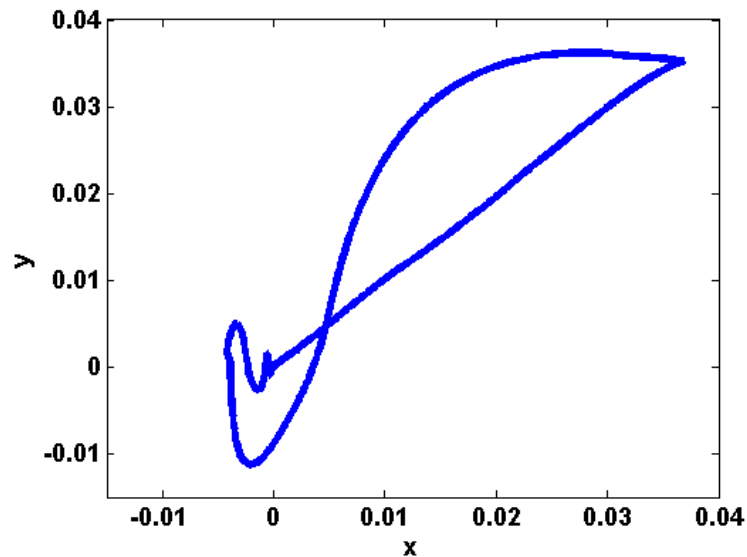

Figure 34: CoM trajectory ($F = 25N$ and $\alpha = \pi/4$)

The final simulation is applied to see the effect of the absence of an ankle strategy. In this simulation, the robot is pushed with the same force $(F = 30N, \alpha = \pi/4)$., but without application of any strategy. The results are shown in Fig. 35. In this case, the robot bounces first to the front then to the back and then it finally falls on its back.
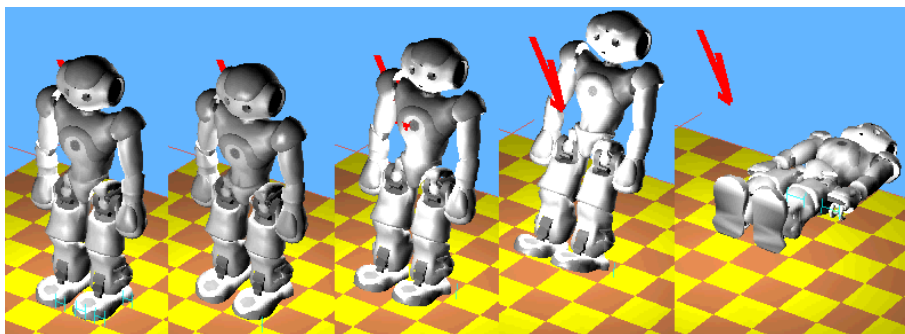

Figure 35: Webots simulation without a strategy ($F = 30N$ and $\alpha = \pi/4$)

2. *Hip Strategy*

In this section, the hip strategy is simulated on Webots. Fig. 36 shows snapshots of this strategy. The robot is pushed with 35 *N* of force for 0.1 *s* oriented at $\pi/4$. The frames show how the robot bends over, in the same direction of the push, to recover.
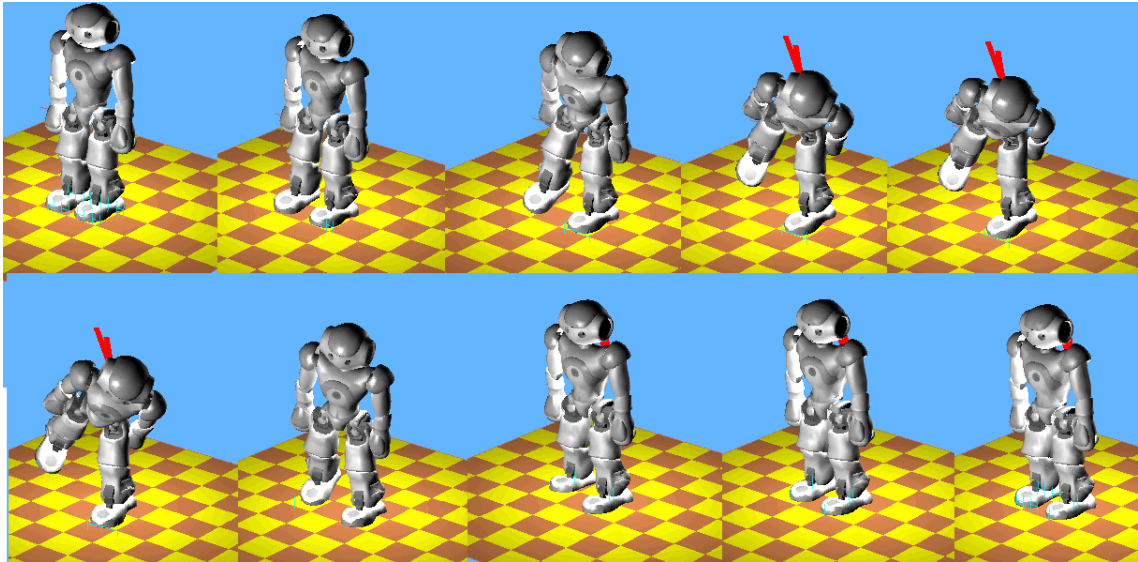

Figure 36: Webots simulation for a 35 *N* of force at an angle $\alpha = \pi/4$

Fig. 37 shows the hip division volume and the outcome of this simulation. As expected, all the states of the robot are within the hip decision volume.
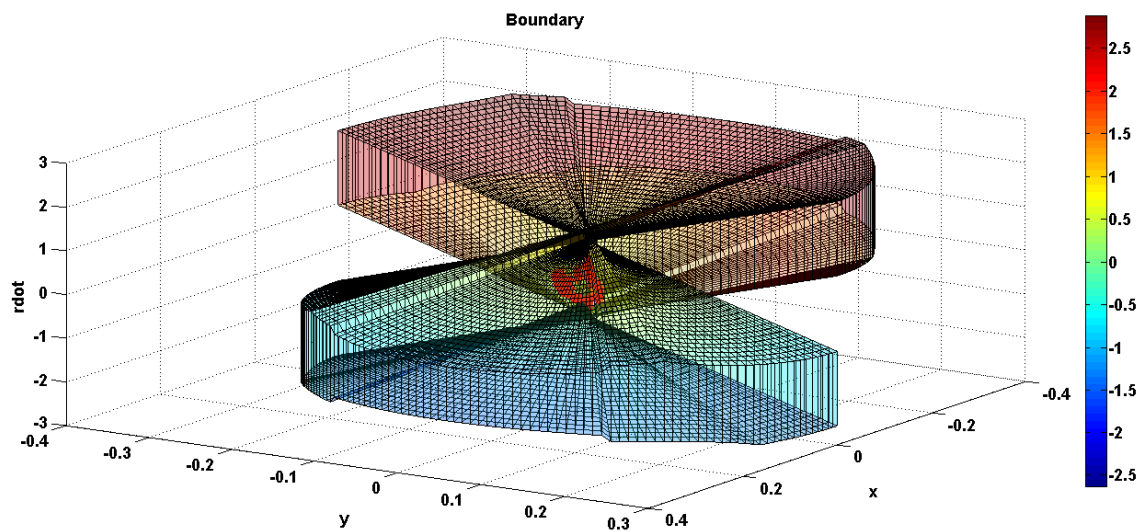

Figure 37: Hip decision volume of Webots simulation for a 35*N* of force at an angle $\alpha = \pi/4$

The next two simulations are done by pushing the simulated robot from its right side with a force of $31N$ for $0.1s$. In the first scenario, the robot fails to recover using the ankle strategy. The push increases the robot's velocity until the states move out of the decision volume at $(0m, 0.024m, 0.472m/s)$. After that, all points remain outside the decision volume and the robot fails to recover (Fig. 38). Although there is a temporary deceleration due to the ankle strategy, after the robot exits the decision volume, the deceleration turns into acceleration. As a result, the robot cannot return to its state of equilibrium. The CoM exceeds the support polygon, and it moves further away from the decision volume.
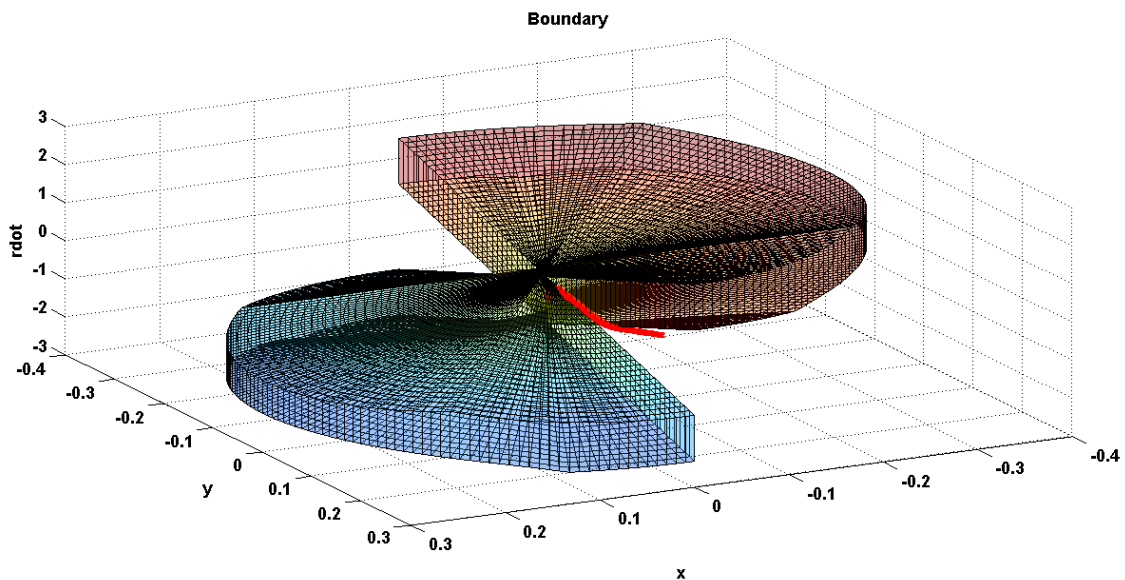

Figure 38: Decision volume for the ankle strategy with $31N$ push from the right

In the next scenario, the left ankle and the left hip are involved in the robot recovery from the same disturbance described previously. In that case the hip is accelerated in the same direction of the push (Fig. 40). In this scenario, the robot is able to recover from the $31N$ push that previously caused the fall. Fig. 39 shows the hip decision volume enclosing the robot state curve. By examining this curve, in the first phase the robot accelerates because it is pushed. Then afterwards it decelerates until it changes direction, reaches its equilibrium, and stops. This shows the importance of the hip strategy.
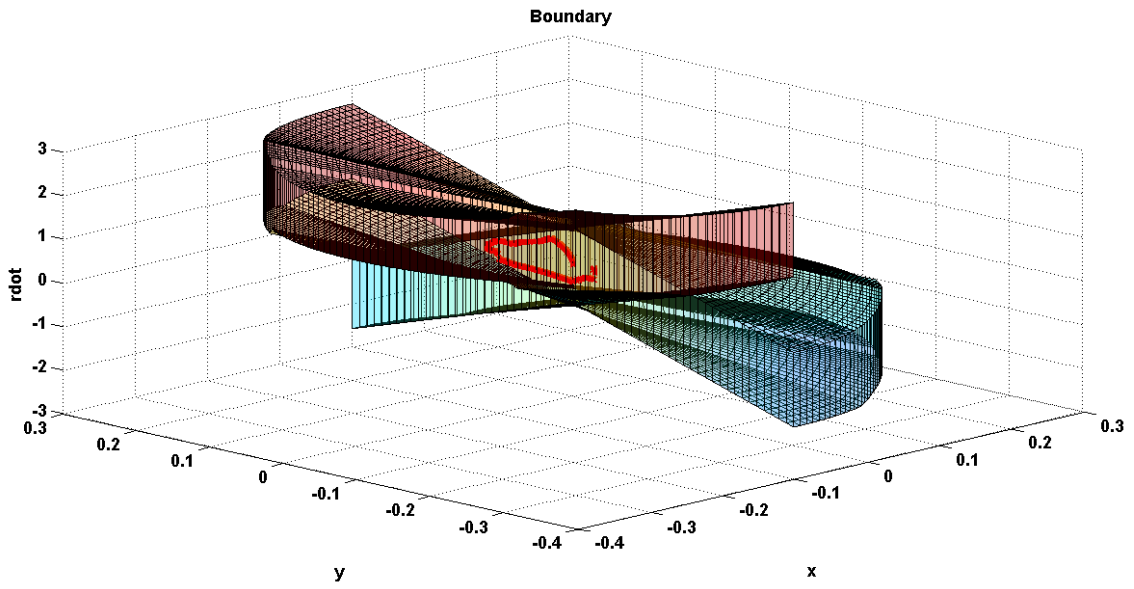
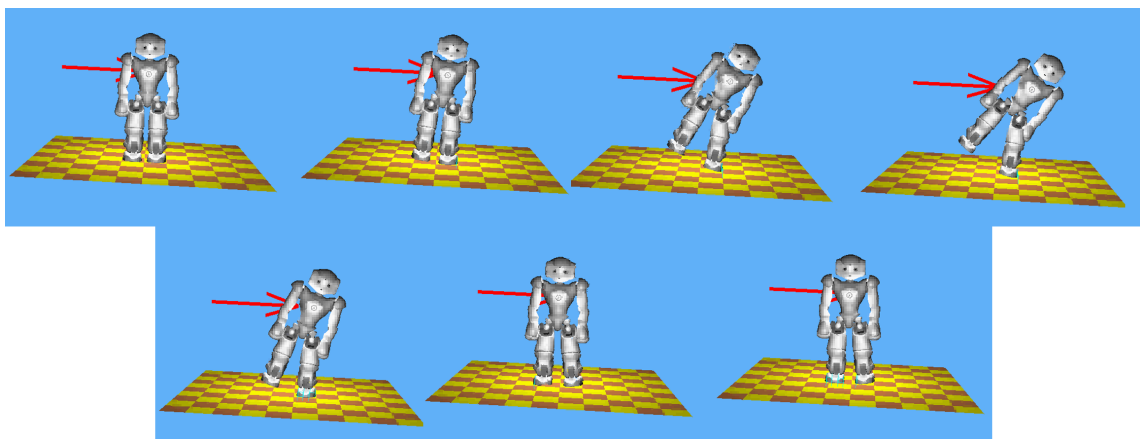Figure 39: Decision volume for the hip strategy with 31N push from the right

Figure 40: Webots simulation of the hip strategy with a 31N force form the right

C. Implementation

In the following sections, the strategies are implemented on a real humanoid, which is the NAO robot.

1. Ankle Strategy

In this experiment, the robot is struck by a ball, which imparts a disturbance force of 46.5 N as measured by a force sensor. The NAO robot reacts using the ankle strategy only. After an examination of the snapshots in fig. 41, it becomes apparent that the robot's left foot partially loses contact with the ground. In this case, the right foot is the main foot responsible for the strategy implementation.
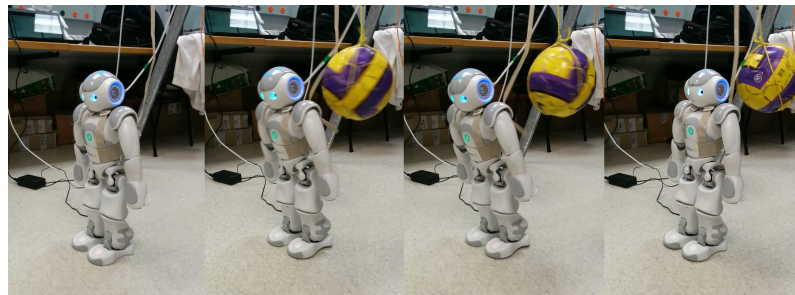

Figure 41: Ankle strategy applied to real robot

When the robot is pushed by the ball, the CoM moves 0.056 m to the front and 0.02 m to the right as shown in Fig. 42 and Fig. 43 respectively. These values are consistent with the ball direction, since the ball is coming from the back left side.
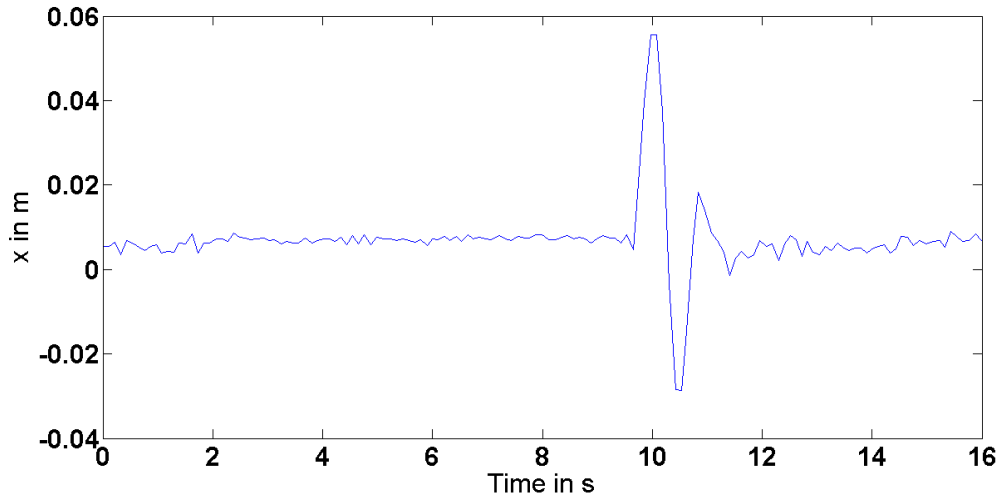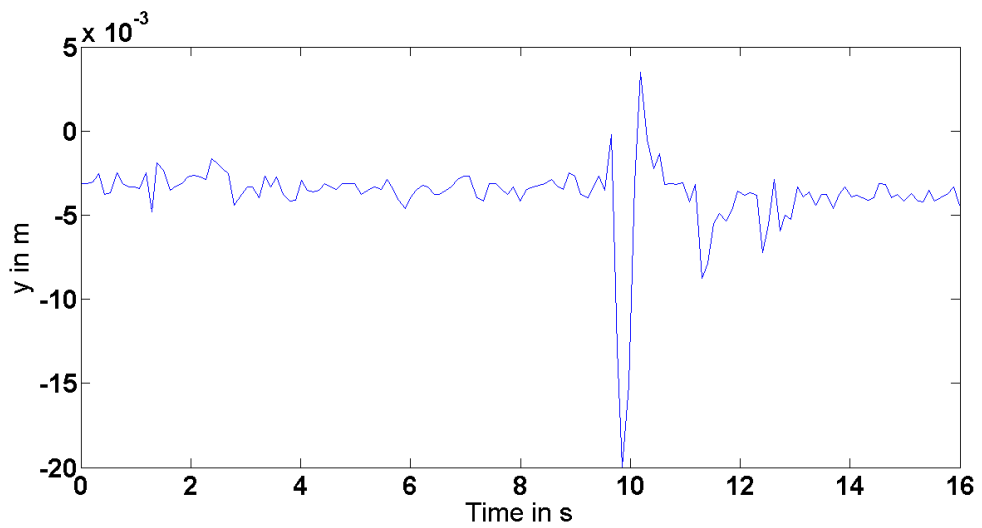
Figure 42: x_{CoM} in function of time

Figure 43: y_{CoM} in function of time
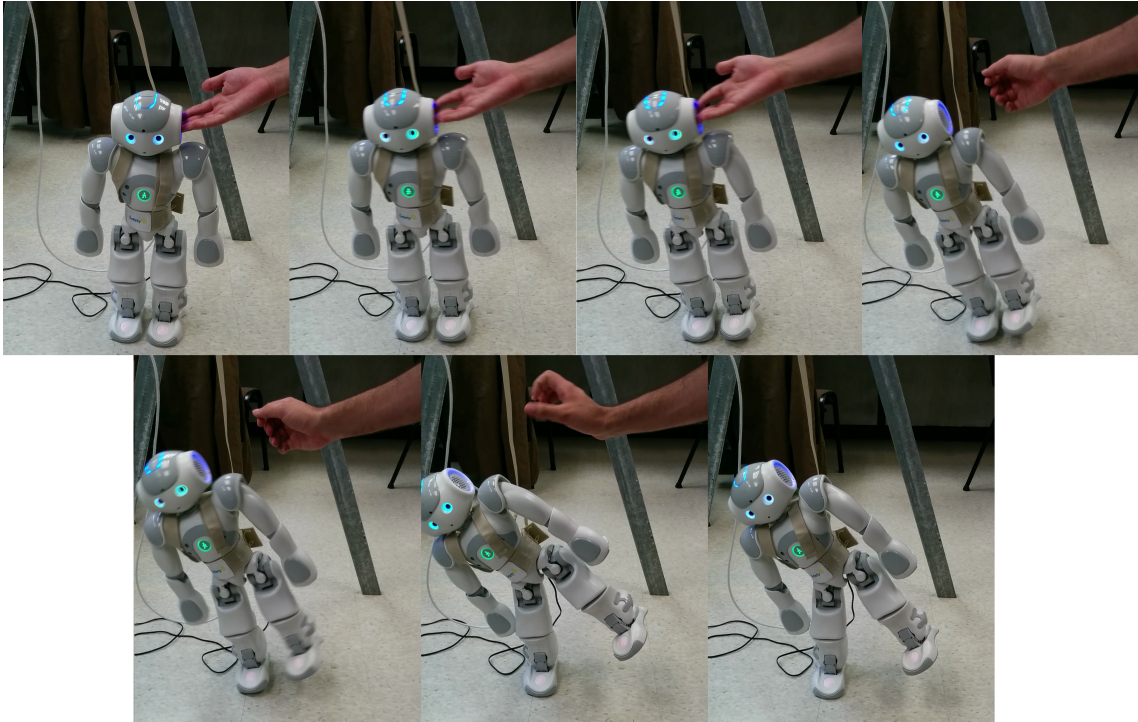
2. *Hip Strategy*

Figure 44: Hip strategy applied to the real robot

In this experiment, the robot is pushed from its left side. Fig. 44 shows a snapshot of the hip strategy. In this case, the push is done manually. Then, when it exceeds the ankle decision volume, the right hip is activated. The torso rotates in the counterclockwise direction. After implementing the hip strategy, the robot balance is only maintained by the right ankle.

Fig. 45 shows the variation of the CoM position y and the velocity $\dot{y}$ in function of time. After the robot is pushed, its velocity increases in the negative direction until it reaches a value of $\dot{y} = -0.26m/s$ at $y = -0.095m$. This point is beyond the ankle decision volume. Hence, the hip strategy is activated. When the hip torque is applied, the velocity changes abruptly until it reaches a value of $\dot{y} = 0.21m/s$. At that point, the hip stops and the velocity decrease to $\dot{y} = -0.05m/s$. Finally, the ankle strategy takes over causing some oscillation before the CoM is finally centered over the robot's right foot.

Unfortunately, the implementation of the hip strategy was only limited to the
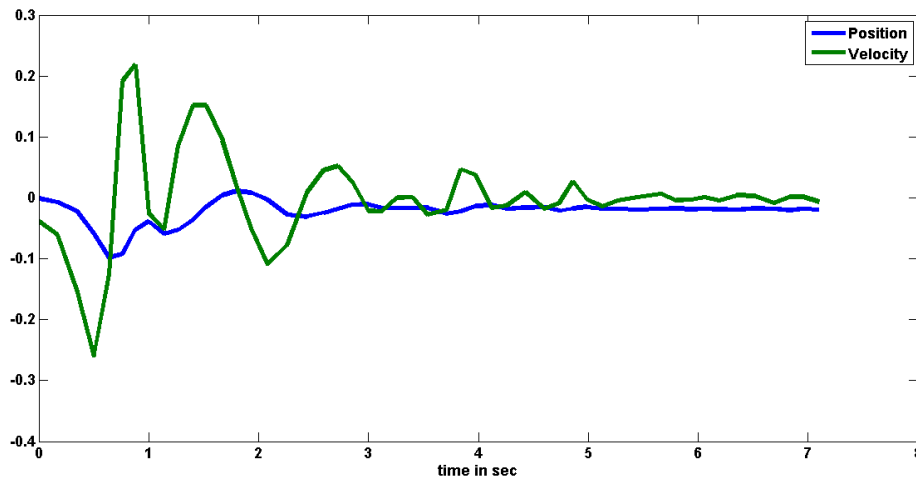
Figure 45: Position in *m* (blue) and velocity in *m/s* (green) of the CoM of the robot in the *y*-direction

sideway motion. This is caused by the maximum ankle motor pitch torque that was not sufficient for the strategy implementation. In other words, one ankle pith motor is not enough to hold the entire robot mass. The robot ankles can provide a maximum amount of $\tau_{max} = 2.1N.m$, whereas in the Webots simulator the torque value reaches a peak of $7.4N.m$, which is larger than $2.1N.m$. In addition, the ankle pitch can hold the robot mass statically along the *x*-direction at $x_{max} = \tau_{max}/mg = 0.042m$, whereas in the simulation the CoM reaches a larger value. In the case of the real robot, beyond $0.042m$ the robot falls because the motor cannot hold the robot mass. Finally the robot motor was tested by starting from different *x* values and programing the ankle pitch motor to set *x* back to zero. For values less than $0.04m$ the robot did not provide enough torque and the robot remained static, whereas for larger values of *x*the robot felt down.

CHAPTER VI

CONCLUSION

The work done in this thesis is a progression of previous work done on humanoid fall avoidance. To adapt in a dynamic environment, humanoids need to be programmed to handle sudden external random perturbations. This work presents two fall avoidance strategies, which are the ankle strategy and the hip strategy that handle perturbations coming from random directions. This is one-step forward toward fall avoidance for humanoids.

For a robot to handle a push from a random direction, two strategies were developed. These strategies, which are physically modeled, are based on human reaction and response for push recovery. For each strategy, a decision volume is constructed analytically from the stable states of the robot. These states are the CoM position and velocity from which the robot can restore its balance using one of the two strategies. The appropriate strategy can be selected depending on the location of the robot states in the decision volume.

By comparing the decision volume to what is known in the literature as decision surface, it can be noted that the decision volume is a generalization of the decision surface, where perturbation from different direction can be identified. On the other hand, the decision surface it is limited to one direction, which is in the sagittal or coronal plane. In addition, the decision surface is a part contained in the decision volume, and can be seen at $\alpha = 0$ for the sagittal plane and $\alpha = \pi/2$ for the coronal plane.

Our future work may include fine-tuning of these decision volumes using machine learning. This compensates for the assumptions made, which are the constant height of the CoM and the sphere that models the upper body. Regarding the

implementation, a robot with a closed loop force control on its joint has the ability to apply the VMC theory with more accuracy. Also a robot with compliant joints [40], will imitate human joints better.

BIBLIOGRAPHY

[1] Wael Suleiman, Fumio Kanehiro, Kanako Miura, and Eiichi Yoshida. Improving zmp-based control model using system identification techniques. In *Humanoid Robots, 2009. Humanoids 2009. 9th IEEE-RAS International Conference on*, pages 74–80. IEEE, 2009.

[2] J.J. Craig. *Introduction to Robotics: Mechanics and Control.* Addison-Wesley series in electrical and computer engineering: control engineering. Pearson Education, Incorporated, 2005.

[3] Kei Okada, Mitsuharu Kojima, Yuuichi Sagawa, Toshiyuki Ichino, Kenji Sato, and Masayuki Inaba. Vision based behavior verification system of humanoid robot for daily environment tasks. In *Humanoid Robots, 2006 6th IEEE-RAS International Conference on*, pages 7–12. IEEE, 2006.

[4] Fabien Gravot, Atsushi Haneda, Kei Okada, and Masayuki Inaba. Cooking for humanoid robot, a task that needs symbolic and geometric reasonings. In *Robotics and Automation, 2006. ICRA 2006. Proceedings 2006 IEEE International Conference on*, pages 462–467. IEEE, 2006.

[5] Tiffany L Chen and Charles C Kemp. Lead me by the hand: evaluation of a direct physical interface for nursing assistant robots. In *Proceedings of the 5th ACM/IEEE international conference on Human-robot interaction*, pages 367–374. IEEE Press, 2010.

[6] David A Winter. Human balance and posture control during standing and walking. *Gait & posture*, 3(4):193–214, 1995.

[7] Ryosuke Chiba, Hiroaki Ogawa, Kaoru Takakusaki, Hajime Asama, and Jun Ota. Muscle activities changing model by difference in sensory inputs on human posture control. In *Intelligent Autonomous Systems 12*, pages 479–491. Springer, 2013.

[8] Jerry Pratt, Chee-Meng Chew, Ann Torres, Peter Dilworth, and Gill Pratt. Virtual model control: An intuitive approach for bipedal locomotion. *The International Journal of Robotics Research*, 20(2):129–143, 2001.

[9] Webots. http://www.cyberbotics.com. Commercial Mobile Robot Simulation Software.

[10] Aldebaran-Robotics. http://www.aldebaran-robotics.com/en/. French Robotics Company.

[11] Jerry E Pratt and Sergey V Drakunov. Derivation and application of a conserved orbital energy for the inverted pendulum bipedal walking model. In *ICRA*, pages 4653–4660, 2007.

[12] N Kofinas. Forward and inverse kinematics for the nao humanoid robot. Master's thesis, Technical University of Crete, Greece, July 2012.

[13] Miomir Vukobratović et al. Dynamics of biped locomotion. In *Biped Locomotion*, pages 1–52. Springer, 1990.

[14] Pieter van Zutven, Dragan Kostic, and Henk Nijmeijer. Modeling, identification and stability of humanoid robots. Master's thesis, Master thesis, DCT 2009.100. Eindhoven University of Technology, 2009.

[15] Miomir Vukobratović and Branislav Borovac. Zero-moment pointâĂŤthirty five years of its life. *International Journal of Humanoid Robotics*, 1(01):157–173, 2004.

[16] Reimund Renner and Sven Behnke. Instability detection and fall avoidance for a humanoid using attitude sensors and reflexes. In *Intelligent robots and systems, 2006 IEEE/RSJ international conference on*, pages 2967–2973. IEEE, 2006.

[17] Philippe Sardain and Guy Bessonnet. Forces acting on a biped robot. center of pressure-zero moment point. *Systems, Man and Cybernetics, Part A: Systems and Humans, IEEE Transactions on*, 34(5):630–637, 2004.

[18] M. Vukobratovic and B. Borovac. Zero-moment point, thirty five years of its life. *International Journal of Humanoid Robotics*, 18:157–173, 2007.

[19] H. Hemami, C. Wall, F. Black, and G. Golliday. Single inverted pendulum biped experiments. *Journal of Interdisc. Model. and Simul.*, 2(3), 1979.

[20] Shuuji Kajita and Kazuo Tani. Study of dynamic biped locomotion on rugged terrain-derivation and application of the linear inverted pendulum mode. In *Robotics and Automation, 1991. Proceedings., 1991 IEEE International Conference on*, pages 1405–1411. IEEE, 1991.

[21] Shuuji Kajita, Fumio Kanehiro, Kenji Kaneko, Kiyoshi Fujiwara, Kensuke Harada, Kazuhito Yokoi, and Hirohisa Hirukawa. Biped walking pattern generation by using preview control of zero-moment point. In *Robotics and Automation, 2003. Proceedings. ICRA'03. IEEE International Conference on*, volume 2, pages 1620–1626. IEEE, 2003.

[22] Taku Komura, Howard Leung, Shunsuke Kudoh, and James Kuffner. A feedback controller for biped humanoids that can counteract large perturbations during gait. In *Robotics and Automation, 2005. ICRA 2005. Proceedings of the 2005 IEEE International Conference on*, pages 1989–1995. IEEE, 2005.

[23] Shunsuke Kudoh and Taku Komura. C 2 continuous gait-pattern generation for biped robots. In *Intelligent Robots and Systems, 2003.(IROS 2003). Proceedings.*

2003 IEEE/RSJ International Conference on, volume 2, pages 1135–1140. IEEE, 2003.

[24] Benjamin Stephens. Humanoid push recovery. In *Humanoid Robots, 2007 7th IEEE-RAS International Conference on*, pages 589–595. IEEE, 2007.

[25] Jerry Pratt, John Carff, Sergey Drakunov, and Ambarish Goswami. Capture point: A step toward humanoid push recovery. In *Humanoid Robots, 2006 6th IEEE-RAS International Conference on*, pages 200–207. IEEE, 2006.

[26] David A Winter, Aftab E Patla, Shirley Rietdyk, and Milad G Ishac. Ankle muscle stiffness in the control of balance during quiet standing. *Journal of Neurophysiology*, 85(6):2630–2633, 2001.

[27] Twan Koolen, Tomas De Boer, John Rebula, Ambarish Goswami, and Jerry Pratt. Capturability-based analysis and control of legged locomotion, part 1: Theory and application to three simple gait models. *The International Journal of Robotics Research*, 31(9):1094–1113, 2012.

[28] Jerry Pratt, Twan Koolen, Tomas De Boer, John Rebula, Sebastien Cotton, John Carff, Matthew Johnson, and Peter Neuhaus. Capturability-based analysis and control of legged locomotion, part 2: Application to m2v2, a lower-body humanoid. *The International Journal of Robotics Research*, 31(10):1117–1133, 2012.

[29] John Rebula, Fabian Canas, Jerry Pratt, and Ambarish Goswami. Learning capture points for humanoid push recovery. In *Humanoid Robots, 2007 7th IEEE-RAS International Conference on*, pages 65–72. IEEE, 2007.

[30] B.Stephens. Humanoid push recovey. *Proceedings of the IEEE/RSJ conference on Intelligent Robots and Systems*, 2007.

[31] Bassam Jalgha and Daniel C Asmar. A simple momentum controller for humanoid push recovery. In *Advances in Robotics*, pages 95–102. Springer, 2009.

[32] Bassam Jalgha, Daniel Asmar, and Imad Elhajj. A hybrid ankle/hip preemptive falling scheme for humanoid robots. In *Robotics and Automation (ICRA), 2011 IEEE International Conference on*, pages 1256–1262. IEEE, 2011.

[33] Daniel C Asmar, Bassam Jalgha, and Adel Fakih. Humanoid fall avoidance using a mixture of strategies. *International Journal of Humanoid Robotics*, 9(01), 2012.

[34] Akinori Nishio, Kentaro Takahashi, and Dragomir N Nenchev. Balance control of a humanoid robot based on the reaction null space method. In *Intelligent Robots and Systems, 2006 IEEE/RSJ International Conference on*, pages 1996–2001. IEEE, 2006.

[35] Dragomir N Nenchev and Akinori Nishio. Ankle and hip strategies for balance recovery of a biped subjected to an impact. *Robotica*, 26(5):643–653, 2008.

[36] Dragomir N Nenchev and Kazuya Yoshida. Impact analysis and post-impact motion control issues of a free-floating space robot subject to a force impulse. *Robotics and Automation, IEEE Transactions on*, 15(3):548–557, 1999.

[37] Shuuji Kajita, Fumio Kanehiro, Kenji Kaneko, Kazuhito Yokoi, and Hirohisa Hirukawa. The 3d linear inverted pendulum mode: A simple modeling for a biped walking pattern generation. In *Intelligent Robots and Systems, 2001. Proceedings. 2001 IEEE/RSJ International Conference on*, volume 1, pages 239–246. IEEE, 2001.

[38] S. Kajita, O. Matsumoto, and M. Saigo. Real-time 3d walking pattern generation for a biped robot with telescopic legs. In *Robotics and Automation (ICRA), IEEE International Conference on*, number 2299-2308, 2001.

[39] Jerry E Pratt. Exploiting inherent robustness and natural dynamics in the control of bipedal walking robots. Technical report, DTIC Document, 2000.

[40] Luca Colasanto, Nikos G Tsagarakis, and Darwin G Caldwell. A compact model for the compliant humanoid robot coman. In *Biomedical Robotics and Biomechatronics (BioRob), 2012 4th IEEE RAS & EMBS International Conference on*, pages 688–694. IEEE, 2012.